INSTITUTE OF PHYSICS
FACULTY OF PHYSICS, ASTRONOMY
AND APPLIED COMPUTER SCIENCE
JAGIELLONIAN UNIVERSITY

Master Thesis

Studies of detection of γ radiation with use of organic scintillator detectors in view of positron emission tomography

Szymon Niedźwiecki

Supervisor: Prof. Paweł Moskal

Cracow, 2011

Acknowledgments

Abstract

Studies of detection of γ radiation with use of organic scintillator detectors in view of positron emission tomography

Positron emission tomography (PET) is experiencing nowadays a lot of interest. PET scanner measures density distribution of radiopharmaceuticals with radioactive isotopes emitting positrons in human body. annihilation of positrons with electrons from the body of the patient results in emission of two gamma quanta, going back to back which are then measured in detectors surrounding the patient. After applying reconstruction algorithms density distribution of annihilations is determined. PET modalities can effectively vizualize metabolic processes inside examined patient, unlike other kind of scans like Computer Tomography or Nuclear Magnetic Resonance, which tell us only about anatomy of the patients body.

In recent times even more sophisticated method of scan was introduced - the Time-Of-Flight PET. TOF PET measures time difference between arrival of gamma quanta in two detectors. Hovewer due to lack of fast scintillaton materials this method weren't applied in practice. Availability of new, faster scintillators and cost-effective photomultipliers, as well as improvements in field of electronics enabled usage of TOF PET modalities. Resolution of measuring time difference influences spatial resolution of reconstruction thus making this quantity most important when designing TOF PET scanner. One of the best presently available scanner achieved time resolution of about 550 ps.

In this thesis feasibility study of using plastic scintillators in TOF PET reconstruction is tested. At present TOF PET scanners are based on crystal scintillators, which compared to plastic scintillators are much slower and more expensive to manufacture. Measurements of amplitude spectra of polymer scintillators, which were irradiated by gamma quanta from annihilation, made by dr A. Kochanowski and mgr Ł. Kapłon in Chemistry Department of Jagiellonian University, allowed for determining best composition of base, primary and secondary additive. As a result of the test performed in the framework of this thesis a PVT+PPO+POPOP was found as the best combination out of eight examined. Experimental measurement of distrubution of time difference between signals from both sides of RP422 scintillator strip has been also performed with result of ~ 680 ps. This result can be further improved by upgrading electronic components of experimental setup.

Streszczenie

Badanie detekcji promieniowania gamma za pomocą organicznych detektorów scyntylacyjnych pod kątem ich wykorzystania w pozytonowej tomografii emisyjnej

Skanery PET pozwalają na nieinwazyjne obrazowanie rozkładu gęstości farmaceutyków w ciele pacjenta. W tym celu farmaceutyki znakowane są radioaktywnymi izotopami emitującymi pozytony. W wyniku anihilacji pozytonów i elektronów z ciała pacjenta, emitowane są dwa kwanty gamma, poruszające się w przeciwnych kierunkach, które następnie są mierzone w detektorach otaczających pacjenta. Po zastosowaniu algorytmów rekonstrukcji określany jest rozkład gęstości miejsc anihilacji.

W ostatnim czasie zostały wprowadzone jeszcze bardziej wyrafinowane metoda skanowania. TOF PET (z ang. Time of Flight) mierzy różnicę czasów pomiędzy pojawieniem się dwóch kwantów gamma w detektorach. Niestety brak szybkich materiałów scyntylacyjnych uniemożliwiłwykorzystanie tych skanerów w praktyce. Dostępność nowych, szybszych scyntylatorów oraz postępy w polu elektroniki a także większy wybór opłacalnych fotopowielaczy pozwoliły powrót do badań nad skanerami TOF PET. Dokładność zmierzenia różnicy czasów wpływa na rozdzielczość przestrzenną rekonstrukcji, sprawiając, że jest to najważniejsza wielkość brana pod uwagę przy projektowaniu skanerów TOF PET. Jeden z najlepszych, obecnie dostępnych skanerów posiada rozdzielczość czasową około 550 ps.

W tej pracy badana jest możliwość wykorzystania plastikowych scyntylatorów w budowie skanera TOF PET. Obecne skanery TOF PET są zbudowane z kryształów scyntylacyjnych, które w porównaniu z plastikowymi scyntylatorami są o wiele wolniejsze i droższe w produkcji. W ramach tej pracy wykonano pomiary widm amplitud scyntylatorów polymerowych naświetlanych kwantami anihilacyjnymi, wykonanych przez dr A. Kochanowskiego i mgr Ł. Kapłona na wydziale Chemii Uniwersytetu Jagiellońskiego. Wyniki pomiarów pozwoliły na wyznaczenie najlepszej mieszanki bazy, pierwszego dodatku i drugiego dodatku, do wykorzystania w budowie pasków polymerowych dla paskowego TOF PET. Wykonany został także pomiar dystrybucji różnicy czasów pomiędzy sygnałami z dwóch stron paska scyntylatora RP422. Uzyskany wynik to $\sigma \sim 680$ ps. W przyszłości rozdzielczość ta będzie poprawona poprzez zastosowanie ulepszonych układów elektronicznych.

Contents

Chapter 1

Introduction

Positon emission tomography (PET) is experiencing nowadays a lot of interest. This examination allows to find spatial and temporal distributions of chosen substances inside human body. In over 30 years since first tomography ring was used, we have learned that PET modalities can effectively visualize metabolic processes inside examined patient, unlike other kind of scans like Computer Tomography or Nuclear Magnetic Resonance, which tell us only about anatomy of body. As noted in [1] PET allows for diagnosis of many diseases in early stage [2, 3]. For example it gives information about concentration of cancer cells, which have different metabolism than normal cells; cardiac problems, or changes in brains of people with mental diseases. PET scanner measures the density distribution of radiopharmaceuticals with radioactive isotopes emitting positrons. annihilation of positrons with electrons from the body of the patient results in emission of two gamma quanta, going back to back which are then measured in detectors surrounding the patient. After applying reconstruction algorithms the density distribution of annihilations is determined.

In recent times even more sophisticated method of scan was introduced - the Time-Of-Flight PET. TOF PET measures time difference between arrival of gamma quanta in two detectors. The idea to use TOF was proposed in early stages of PET developement [4] and first TOF PET scanner was made in 1980s [4]. Those early scanners were made of CsF or BaF_2 crystals which could handle high-count-rates in research of brain and heart by using short lived isotopes [4]. However those detectors could not match at that time in field of spatial resolution and sensivity with BGO crystals used in PET scanners. This led to obviating from this kind of examination.

Availability of new scintillators (like LSO and LYSO) [5, 6], as well as improvements in the field of electronics and more choices of cost-

effective photomultipliers made studies on TOF PET available again. In 2005 Siemens TOF PET scanner based on LSO achieved 1.2 ns timing resolution [8], a first commercial TOF PET was constructed in 2006 by Philips and was based on LYSO crystals, this scanner achieved 650 ps resolution time, later in in 2007 Gemini TF scanner based on LYSO crystals achieved even better result - 600 ps [4] and finally in 2008 Simens made a prototpye scanner based on LSO crystals that achieved 550 ps. Spatial resolution of TOF PET scanner is directly connected with time resolution of detectors used, which makes it the most important parameter that charaterizes TOF PET scanner. It tells how well one can locate the point of annihilation using time difference between two detectors. Time resolution depends on several factors: type of scintillation material, its shape, type of photomultiplier and electronics used to analyse signals. At present all TOF PET scanners use crystal scintillators to detect γ quanta [1]. Shorter rise and decay times of new crystal detector results in better time resolution. Because of that a lot of effort is concentrated on making crystals with as fast signals as possible. In 2010 D. Schaart and collaborators achieved 100 ps (FWHM) time resolution using BrilLance380 (LaBr$_3$:Ce) crystal [7]. Still, those results where achieved only for a very small (3 mm x 3 mm x 5 mm) sample and for a narrow range of amplitudes, smaller than in typical tomographs, and in addition the efficiency for photoelectric absorbtion in this crystal is few times smaller than in LSO or BGO [8]. Information about the time of arrival of gamma quanta in two detectors allows also to reduce propagation of noise along the line of propagation of gamma quanta. Reduction of noise results in increase of sensivity [4]. Further improvement of time resolution from 600 to 100 ps would change sensivity gain by about a factor of 6 [4].

Crystal scintillators, currently used as a base in TOF PET scanner, have time resolution limited by long decay time of signals. , On the other hand, plastic scintillators, used for many particle and nuclear physics experiments have faster signals and offer much better time resolutions [9–12]. The aim of this thesis is to perform the first test of the polymer scintillators in view of their application for TOF PET, as suggested in references [13–15].

TOF resolution for plastic scintillators can be even better than 100 ps. This, combined with large light attenuation lenght (about 2 meters), would allow to use 1 meter strips of plastic. One of the proposed solution for TOF PET based on polymer scintillators is a barrel built out of strips [13]. Scintillation light from both sides of each strip would be converted into electric signal by photomultipliers. Barrel made from such strips could allow making a 3D image of the whole body at one

measurement.

In crystal detectors signals from photoelectric effect are used for reconstruction, but in plastic scintillators probability for this phenomenon is negligible. Still it is possible to use events related to Compton effect inside the detector for reconstruction. To compensate for low probability of interaction in plastic, several layers of material can be placed around a patient, each made of plastic strips.

In this thesis study of using plastic scintillators in TOF PET reconstruction is tested. First part of the thesis (chapters 2, 3, 4) contains explanation of TOF PET scanners operation, phenomena connected with this kind of examination, calculations concerning efficiency of detection and simulations of shape of energy spectrum of electrons gained via Compton effect. In second, experimental part (chapters 5 and 6), setups used to measure amplitude spectra of different polymer scintillators and time resolution of RP442 organic scintillator are described. Results from measurements of polymer scintillators allow establishing the best composition of base, primary and secondary additive to be used in making polymer strips for Strip TOF PET. Measurement of distribution of time difference between arrival of signals on both sides RP422 scintillator will give necessary information on time resolution one can reach for gamma quanta of energies equal to 511 keV, origination from annihilation.

In the second chapter of this thesis a brief description of operation of PET detector is posted with more detailed explanation of novel Strip TOF PET scanner based on plastic scintillators.

In the third chapter ways of interaction of γ rays with detectors matter are discussed with emphasis on Compton effect. That chapter includes description of operation method of scintillator detectors and photomultipliers, as well as explanations of differences in light signals origin between organic (plastic) and inorganic (crystal) detectors. The explanation of composition of structure of polymer scintillators is also included.

In the fourth chapter the detector efficiency is calculated as a function of detector thickness for different thresholds of electron energy. Influence of energy resolution on energy spectrum measured by plastic scintillator is also presented. Finally the impact of energy threshold on measured energy spectrum in case of real examination is discussed.

In the fifth chapter experimental setup used for measuring amplitude spectra for different polymer scintillators made in Faculty of Chemistry of the Jagiellonian University and results of those measurements are shown. The best sample is determined and compared with NE102A plastic scintillator. Comparison of doped and pure polymer

scintillators amplitude spectrais also made.

In the sixth chapter studies of time resolution for a strip of RP422 scintillator are presented. Further improvements of obtained time resolution are pointed at the end of the chapter.

This thesis is supplemented with Appendixes describing details of experimental setups and a table with coefficients for photoelectric and Compton effects for LSO, BGO and polymer scintillators.

Chapter 2

Principle of Positron Emission Tomography

Positron emission tomografy (PET) allows measuring spatial distribution of a chosen chemical substance inside patient's body, thus providing information about metabolic processes assiociated with it. Changes in metabolism allow identification of many diseases (e.g. cancer, Parkinson's) and for widening knowledge about changes in brain activity of people with mental disorders. Extensive description of possible applications can be found in [2, 3]. Examination consists of injecting a chemical substance marked with β^+ radioactive isotope and detection of gamma quanta from annihilation of positrons and electrons by a system of scintillator detectors. Data from detectors are used for image reconstruction which gives us information about density distribution of marked chemical substance inside the body of the examined patient.

2.1 Physical basis

On the quark level β^+ decay may be described as a conversion of u quark into d quark with emission of W^+ boson, which decays into positron and neutrino. Because of three-body nature of this decay (n $\rightarrow$ p e$^+$ ν), energy spectrum of positrons is continous in range from zero to maximum energy, which depends on the type of nucleus. Positron moves inside patients body loosing its kinetic energy via interaction with electrons. The e$^+$e$^-$ annihilation occurs predominantly when positron energy decreases to the value of a few keV [16]. One cannot establish the place where β^+ decay occured with better precision than the distance that positron had travelled. This distance depends on type of matter through which positron moves and on the kinetic energy of positron. In case of isotopes used in PET scans positrons

move few milimeters before annihilation [2] (see also Tab. 2.1). This factor constitutes a main limitation of spatial resolution of PET detectors. After losing most of its kinetic energy positron collides with electron forming positronium. This hydrogen-like particle has two stationary states: parapositronium with spins of electron and positron aligned anti-parallelly, and ortopositronium with spins aligned parallelly. Decay time of this system depends on its spin aligment. In first case positronium decays into two γ quanta and in the second case into three. The former occurs in about - 99.7% of cases [17, 18], with γ quanta going back to back.

2.2   Radiopharmaceuticals

Radiopharmaceuticals are chemical substances which are composed of radioactive isotope and a chemical compound used by body in metabolic processes (such as glucose marked with ^{18}F). A few of the most commonly used isotopes are listed in Tab. 2.1. Chemical compound is just a carrier that transports radioactive marker into tissues. Different tissues or metabolic processes can be examined by choosing proper chemical compounds. Production of radioactive isotopes is done by nuclear reactions with light targets and light projectiles [2, 3].

Table 2.1: List of chosen radioisotopes used in PET scans [1, 5]. Shown isotopes are used in radio-pharmaceuticals which play an important role in the metabolism of living organisms [15].

Isotope	Half-time [min.]	Max. energy of positron [keV]	Max. range in tissue [mm]	Average range in water [mm]
^{11}C	20.5	960	4.03	1.7
^{13}N	9.97	1198	5.29	2.0
^{15}O	2	1732	8.12	2.7
^{18}F	109.7	634	2.3	1.4

2.3   PET detectors

Each PET scanner is built from many scintillator detectors forming rings around an examined patient as shown in Fig. 2.1. Presently crystal detectors are used to detect γ rays in all PET scanners.

Gamma quanta, are chosen as ones from the same act of anihillation of positron and electron if they appear in detectors placed opposite to
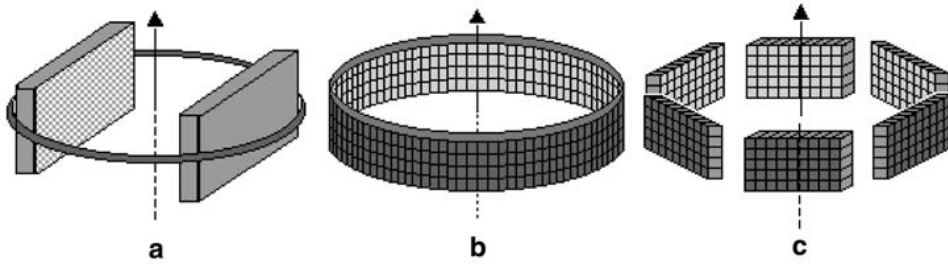
Figure 2.1: Different arrangements of scintillation crystals in PET detectors. Patients lie along lines indicated with arrow. Figure is adapted from [1].

each other in short time (usually 5-10 ns [19]). A single event provides a line between two detectors (LOR: Line Of Response), along which an annihillation occurred (see Fig. 2.2). However using this method it is impossible to find the point of anihillation in the event by event base. Further on, based on the sample of measured LOR one can determine the distribution of radionuclide in different parts of the patient body using advanced reconstruction methods [3].

Figure 2.2: Principle of reconstruction in PET shown in a simplified case where all lines of response originate from one place.

2.4   TOF PET

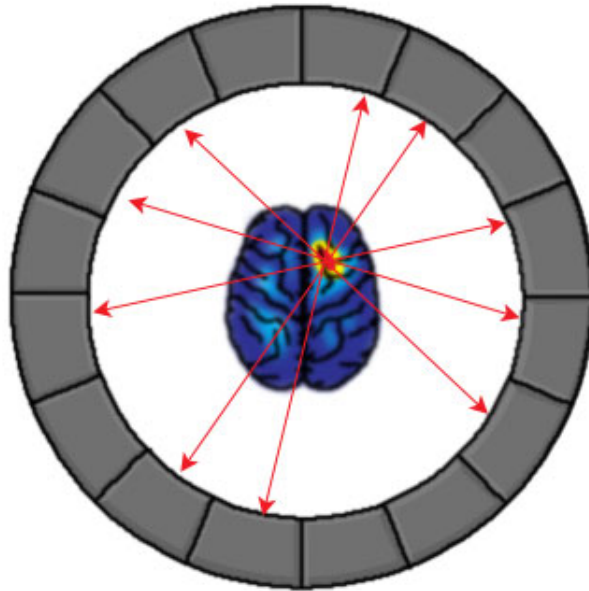Time Of Flight Positron Emmision Tomography (TOF PET) uses difference between the time of flight for gamma quanta from the same annihilation event. The time difference is related to the distance of annihilation point from detectors. As it is indicated schematically in Fig. 2.3. If the source was placed in the center of the ring, the difference of TOFs for detectors A and B would be equal to 0. When the source is moved closer to one of the detectors, the change in position can be derived from the value of difference TOF_A - TOF_B. Accuracy in
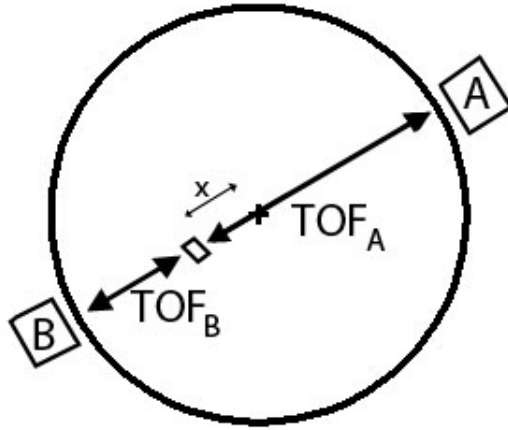
Figure 2.3: TOF PET geometrical model. Annihilation takes place in distance x from the center of the line connecting detectors A and B. TOF_A is proportional to the distance between annihilation point and detector A, TOF_B is proportional to the distance between annihilation point and detector B.

determining localisation is thus limited by the time resolution of those detectors. TOF_A and TOF_B can be expressed as:

$$TOF_A = \frac{x}{c} + \frac{L/2}{c}, \qquad (2.1)$$

$$TOF_B = \frac{L/2}{c} - \frac{x}{c}, \qquad (2.2)$$

where L denotes distance between detectors A and B, c stands for the speed of light and x is the distance between point of annihilation and

the center of the line connecting detectors. Difference between TOFs for two detectors equals:

$$TOF_A - TOF_B = \frac{2x}{c}. \tag{2.3}$$

Localization uncertainty is then expressed as [19]:

$$\Delta x = \frac{c\Delta t}{2}, \tag{2.4}$$

where Δx is localisation error, and Δt denotes time resolution of measuring the time difference between detectors A and B.

In the conventional PET, reconstruction of the image is based on strip across which all volume elements are taken into account, but in TOF PET the region involved in the reconstruction is reduced to only those volume elements which are close to a place identified by the time difference (see Fig. 2.4). Usually a Gaussian distribution is used, which is centered at $x = \frac{c}{2}(TOF_A - TOF_B)$ point with FWHM corresponding to the time resolution.
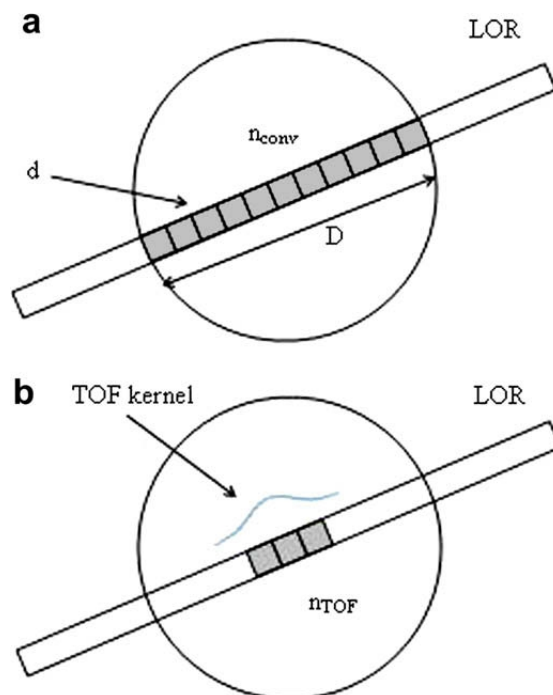

Figure 2.4: Information available from single event registered with a) non-TOF and b) TOF PET detectors. Figure is adapted from [19].

First advantage of this method of reconstruction is that it gives the "true" image faster. Moreover, noise in TOF PET measurements is

18

lower than in non TOF examinations, which is caused by not taking whole lines in reconstruction, but only parts of them, so contribution from backround is much lower. Visual effect of this difference is shown in Fig. 2.5. It shows a picture taken with GEMINI TF TOF PET scanner with time resolution of 585 ps [20]. It is worth to stress that further improvement of the TOF resolution from 550 ps to 100 ps would enhance signal to noise ratio by as much as a factor of 6 [19].
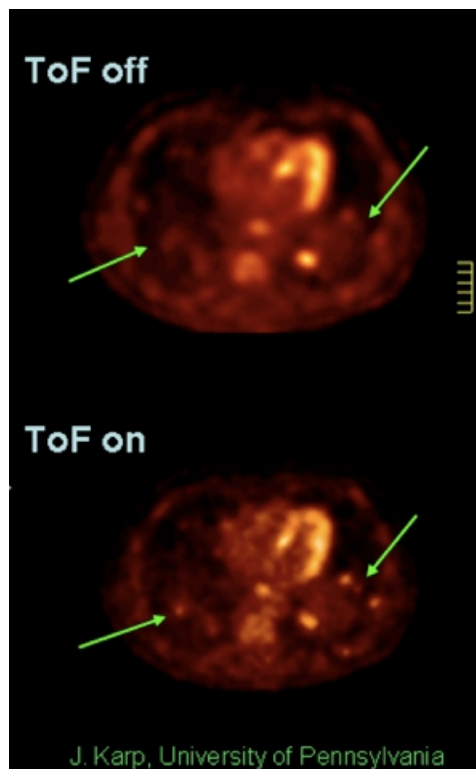
Figure 2.5: Difference in reconstruction with and without TOF. Figure adapted from [4, 21, 22].

As mentioned before, time resolution is the most important parameter that charaterizes a TOF PET scanner. It tells how well one can locate the point of annihilation using time difference between two detectors. Spatial uncertainty as a function of time resolution is shown in Tab. 2.2. Time resolution depends on several factors: type of scintillation material, its shape, type of photomultiplier and electronics used to analyse signal. At present all TOF PET scanners use crystal scintillators to detect annihilation quanta. Shorter rise and decay times of scintillators results in better time resolution. Because of that a lot of effort is concentrated on making crystals with as fast signals

as possible. In 2010 D. Schaart and collaborators achieved 100 ps (FWHM) time resolution using BrilLance380 (LaBr3:Ce) crystal [7]. Still, those results where achieved only for a very small (3 mm x 3 mm x 5 mm) sample and for a narrow range of amplitudes, smaller than in typical tomographs. This crystal has also smaller attenuation coefficient for photoelectric effect than other crystal scintillators used in TOF PET [1].

Another important quantity for improving time resolution is the light output of a material. It is a measure of a number of photons produced in a scintillator per unit of the deposited energy. Most crystal scintillators have light outputs of a few tens of thousands photons per MeV of energy deposited in material.

Table 2.2: Time resolution of the time difference measurement between two detectors and corresponding spatial uncertainty calculated based on equation 2.4.

Time resolution [ns]	Δx [cm]
0.03	0.45
0.05	0.75
0.1	1.5
0.2	3.0
0.3	4.5
0.5	7.5
1.0	15.0
1.2	18.0

2.5 Novel TOF PET solution based on polymer scintillators

Crystal scintillators, besides many advantages such as high probability of photon interaction, high light output and good energy resolution, are very expensive to produce and many of them are hygroscopic. The size of crystal detector is also limited because of short light attenuation lenght. In comparison plastic scintillators are much less expensive and easy to manufacture into many different shapes. TOF resolution for plastic scintillators can be even better than 100 ps. This, combined with large light attenuation lenght (about 2 meters), would allow to use 1 meter strips of plastic. Moreover, plastic scintillators have still large light output of typically 10000 photons/MeV. In PET made of

plastic scintillators, detection chamber would be formed from strips of detectors as shown in Fig. 2.6 [13]. Scintillation light from both sides
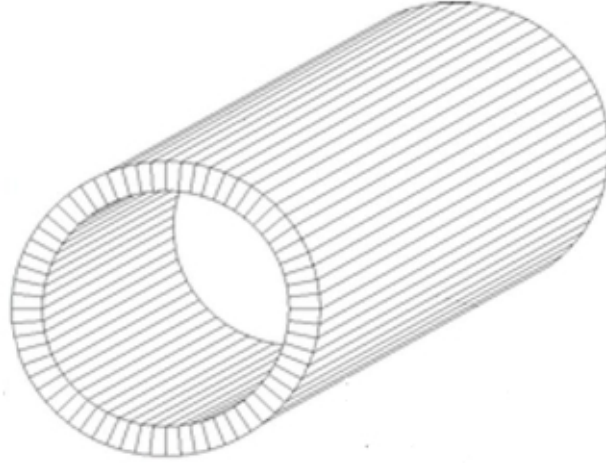

Figure 2.6: Detector arrangement in plastic scintillator PET. Patient would lie inside the barrel, along scintillator strips [13,14].

of each strip is converted into electric signal by photomultipliers. In crystal detectors for reconstruction one uses events from photoelectric effect inside detector, but in plastic scintillators probability for this phenomena is negligible. Still it is possible to use events related to Compton effect inside the detector. The maximum energy deposits of electrons from the Compton edge is equal to about 340 keV. Thus Strip PET with low energy threshold of 200 keV will reduce the scattering of gamma quanta in the body of a patient to the same extent as it is in the currently used tomographs which typically use the low energy threshold of 300 or 350 keV [1]. To compensate for low density of plastic scintillators several layers presented in Fig. 2.6 can be placed around a patient [13, 14]. The total thickness of cylinders of 5 cm results in efficiency of 20% when requiring signals with energy deposits larger than 200 keV.

Determination of impact position of γ ray in one strip and annihilation position is pictorially explained in Fig. 2.7. Strips of scintillators are available in large sizes therefore, it is possible to manufacture detection chamber which would allow for measuring gamma quanta from whole the body at once rather than from a certain parts, significantly decreasing the time of examination. Due to the large solid angle cov-
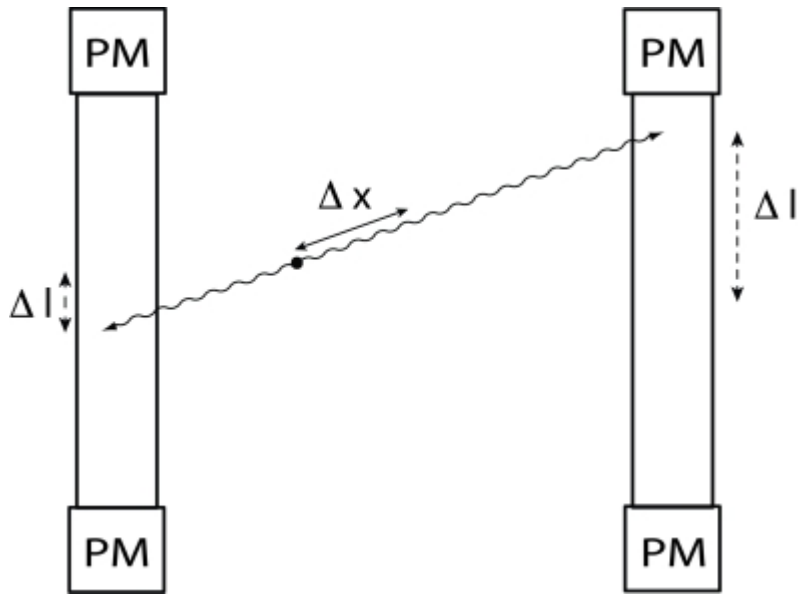
Figure 2.7: Schematic illustration of a new PET concept - Strip PET. The hit position versus the center of the scintillator (Δl) is determined based on time difference measured on both sides of the scintillation strip. Position (Δ x) along the LOR is determined from time difference between two modules [15].

ered and superior TOF resolution, the overall detector efficiency will be increased because of the possibility of effective application of 3D mode of image reconstruction. Overall sensitivity of a 5 cm thick plastic Strip PET with image reconstruction in 3D mode could be even larger than e.g. typical BGO based tomograph with probability for photoelectric effect of 60% used in the 2D mode.

Chapter 3

Interaction of γ rays with detector matter

In general there are many ways of interaction of γ rays with scintillator detectors, but three of them have the highest chance to occur. Those are Compton effect, photoelectric effect and pair creation. In the case of PET, γ quanta posses energies of 511 keV, because they come from annihilation of positron with electron. The threshold energy for pair creation is two times the mass of electron (1022 keV) and this means that for gamma quanta with 511 keV this phenomenon cannot occur. Therefore in the following only photoelectric and Compton effects will be described in more details.

3.1 Photoelectric effect

Photoelectric effect involves absorption of γ ray by bound electron, which results in ejecting the electron from a natom (see Fig. 3.1). Energy conservation law for this reaction can be written as:

$$E_\gamma = T + T_{nuc} + B, \qquad (3.1)$$

where the term on the left part of the equation 3.1 is equal to the energy of γ ray, T denotes kinetic energy of electron, B stands for its bounding energy and T_{nuc} indicates the recoil energy of nucleus. A free electron cannot absorb photon fullfilling both energy and momentum conservation laws. This is why this effect can only occur with bound electrons, where nucleus takes part of momentum as a recoil momentum. The mass of electron is much lower than the mass of the whole nucleus (in case of hydrogen it is $\frac{m_e}{m_p} \approx \frac{1}{2000}$), thus the recoil momentum is very small and can be neglected.
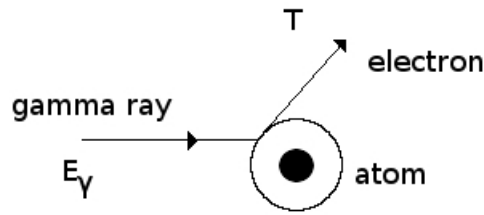
Figure 3.1: Scheme of photoelectric effect. Electron is ejected from an atom after absorption of gamma quantum.
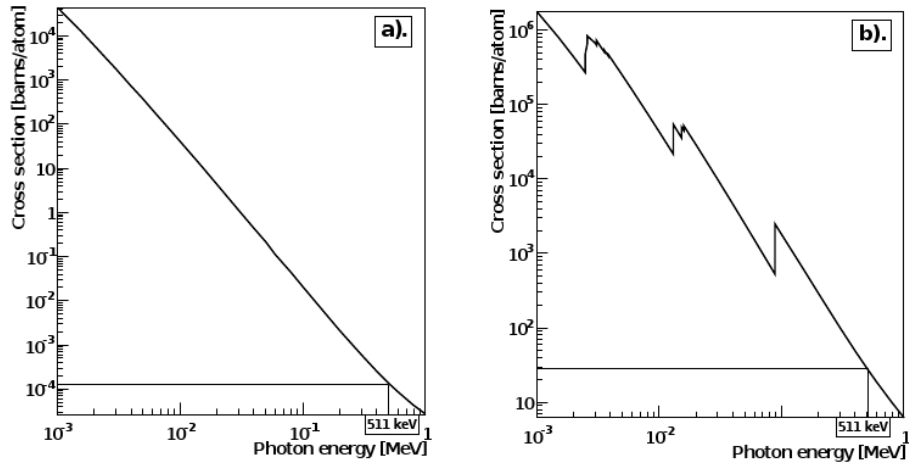
Figure 3.2: Cross section per atom for photoelectric effect as a function of energy for a) carbon and b) lead. Data points are taken from [24]. Cross section for photoelectric effect for energy of γ quanta equal to 511 keV is by more than five orders of magnitude higher for lead than for carbon.

It is difficult to treat photoelectric effect rigorously in theory [23], but generally cross section is a function of the energy of photons and the atomic number of nucleus (number of protons in nuclei) as shown in Fig. 3.2. The dependence of cross section on Z number goes as power of Z to 4th or 5th [23] and is inversely proportional to the power of energy of photons [25]. As can be inferred from comparison of Figs. 3.2 a) and b), with higher energies cross section per atom drops. For certain energies cross section rapidly grows, which happens when energy of γ rays is high enough to free an electron from another, more bound, shell.

From experimental point of view, where one usually cannot change the energy of γ rays, one can try to use material with as high atomic number as possible. In many crystal detectors doping allows for obtaining higher Z number, which increases the probability of photoelectric effect. There are also ongoing investigations of polymer scintillators doped with high Z atoms [26].

3.2 Compton effect

Compton effect is an inelastic scattering of γ rays on quasi-free electrons in matter. Because of the two-body nature of this reaction and axial symmetry of this process, one only needs one variable to describe it. Usually one uses the scattering angle of either electron or γ ray (see Fig. 3.3). Differential cross section for scattering of γ ray in matter, where there is one electron per cm^3 in the solid angle $d\Omega$ has been derived by Klein and Nishima [25]:

$$d\sigma = \frac{r_0^2}{2}(\frac{E}{E_0})^2(\frac{E_0}{E} + \frac{E}{E_0} - \sin^2\varphi)^2 d\Omega, \quad (3.2)$$

where $r_0 = 2,82 \cdot 10^{-13} cm$, E_0 and E are energies of primary and dispersed γ rays, respectively. To obtain cross section for scattering on the whole atom one must multiply this value by the number of electrons (Z number) [25]. Energy distributions of electrons from Compton effect for a few different energies of incoming gamma quanta is shown in Fig. 3.4.
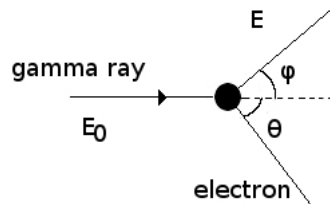

Figure 3.3: Scheme for Compton effect interaction.

These distributions have been derived from equation 3.2 by expressing scattering angle of gamma quantum by the kinetic energy of electron. Connection between these two variables can be expressed as:

$$T = \frac{E_0(1 - cos\varphi)}{\frac{m_e c^2}{E_0} + (1 - cos\varphi)}, \quad (3.3)$$

where T and m_e denote electron kinetic energy and its mass, E_0 is the energy of γ quantum before scattering, and φ stands for the scattering angle defined in Fig. 3.3.
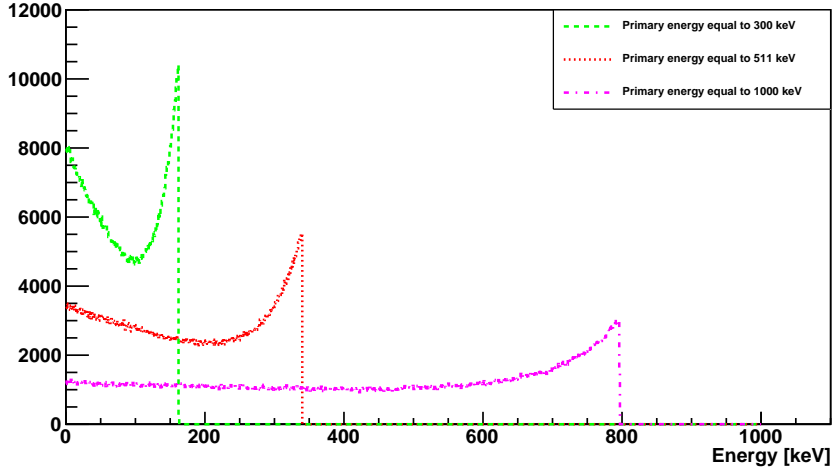
Figure 3.4: Kinetic energy distribution of electrons in Compton effect as a function of primary energy of γ quanta. Enhancement followed by sharp drop at maximum scattering energy of electron is known as Compton edge.

In the Compton process electrons can be scattered in angular range from 0 to 90 degrees, and γ rays in the range from 0 to 180 degrees, where during backscattering one observes maximum kinetic energy for electrons. Relation between maximum kinetic energy of electrons gained through Compton effect and the energy of γ quanta can be described as:

$$T_{max} = E_0 \frac{2 \frac{E_0}{m_e c^2}}{1 + 2 \frac{E_0}{m_e c^2}}, \tag{3.4}$$

and in the case of annihilation quanta with $E_0 = m_e c^2$ this equation reduces further to:

$$T_{max} = \frac{2}{3} E_0. \tag{3.5}$$

3.3 Scintillator detectors

As mentioned before, γ quantum can interact with matter of PET detectors mostly through Compton and photoelectric effects. In both

26

cases electron is produced through one of these interactions. This electron will collide with atoms or molecules in matter, losing a part of its energy in each collision. This process leads to excitation of atoms or molecules to higher energy states or to ionisation. Such interaction will result in excitation of atoms or molecules which will subsequently deexcite into lower energy states via emission of photons with energies equal to the difference between energies of higher and lower energy states. Hence, as a result of interaction of γ rays with scintillator matter light signal is being produced. Typically few tens of thousands photons are emitted per one MeV of energy deposited by the electron.
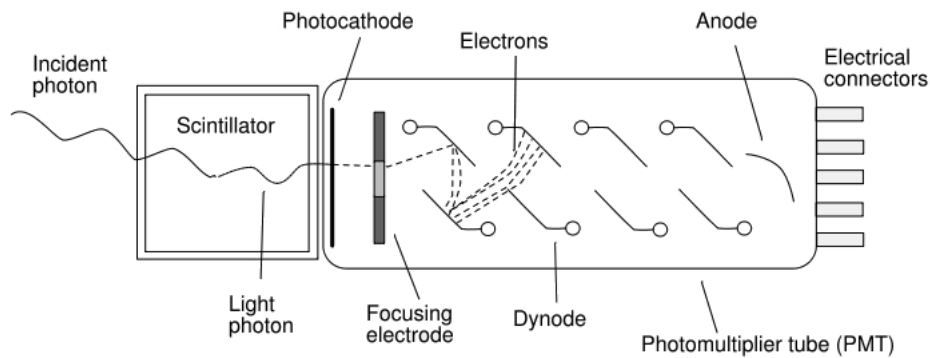
Figure 3.5: Scheme of photomultiplier. Figure is adapted from [5].

Light pulse from scintillator is then converted by photomultiplier into electric signal (see Fig. 3.5). Photons from scintillator material strike the photocatode window, where they produce electrons, via photoelectric effect. Behind the window there is a group of dynodes, each connected to higher and higher voltage. Because of that, between the window and first dynode, as well as between another dynodes there is an electric field. Thus, electrons in this field will be accelerated. While moving from the first to the second dynode, electron will acquire sufficient energy to release few electrons from the second dynode. This effect will be multiplied with each collision. In the end one gets electrons which form electric signal at the output of the photomultiplier.

3.4 Comparison of organic and inorganic scintillators

One can divide scintillation materials into two main groups: made from organic and inorganic substances. Results of measurements depend highly on which type of material one uses. Materials which are made from inorganic substances are mainly crystals. Their main advantage is better energy resolution and greater stopping power which results from higher density and higher atomic number. Main disadvantage of inorganic scintillators is their hygroscopicity and high production costs (because growing of pure crystal without unwanted impurities is very difficult). Light emmision in inorganic scintillators comes from ionisation of the crystals. As shown in Fig. 3.6 electrons can be excited by radiation and thus move from the valence band to the conduction band. This will create an electron-hole pair. Such electrons are no longer bound to individual molecules and can move freely in crystal lattice. Energy required for such phenomenon is higher than width of the forbidden gap (usually 5 eV [1]). A part of the excess energy must be transferred to the crystal via phonons. If a crystal contains impurities they will add a discrete level across the forbidden gap. A hole can ionize one of impurity atoms allowing its electron partner to transit to the excited state and subsequently to the ground state emitting scintillation light.
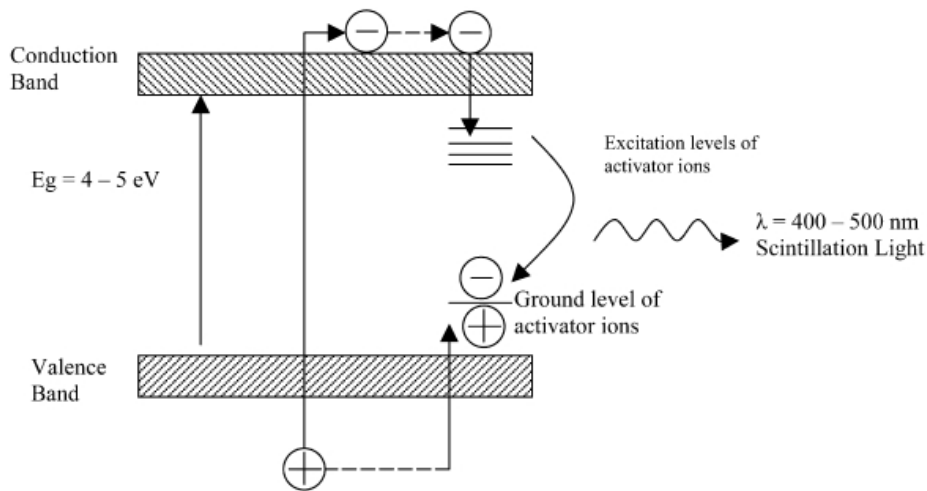

Figure 3.6: The band structure of an inorganic scintillator. The figure is adapted from [1]

In case of organic scintillators light comes from transitions of valence electrons of molecules. Penetrating radiation excites both electron and vibritional levels in molecules [23]. Energy spacing between electron states is of the order of a few eV, while the difference between vibrational states is of the order of a few meV and is shown in Fig. 3.7. Transitions from excited singlet states to vibrational states of the
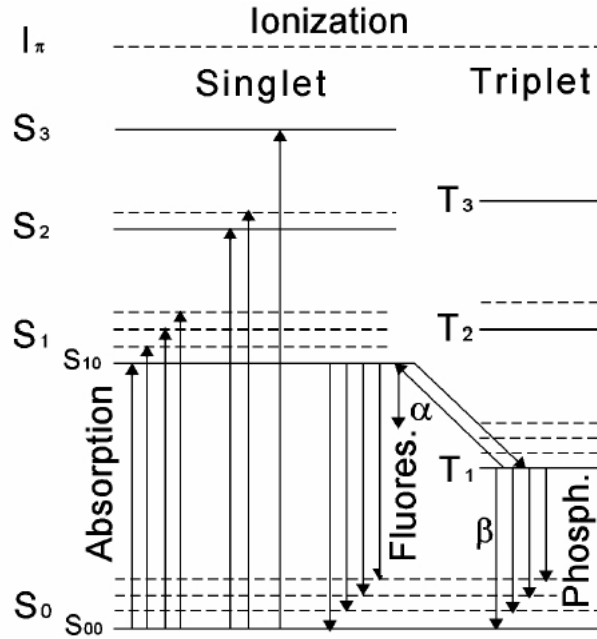
Figure 3.7: The energy levels structure of an organic scintillator molecule. Singlet states are denoted as S, and triplet states as T. Taken from [27].

ground state have high probability for emmision of scintillation light. Similar situation occurs in the case of triplet states transitions, but transitions from triplet to singlet states are usually forbidden by multipole selection rules. Main advantages of organic scintillators are their response time of few ns, while most inorganic ones have ∼40 ns, low production costs and possibilty to make almost any desired shape, while the main disadvantage being low efficiency and negligible probability for photoelectric process. Different properties of scintillator materials are gathered in Tabs. 3.1 and 3.2.

Table 3.1: Properties of scintillator materials

Scintillator name	Type	Density [gm/cm^3]	Light Yield %(NaI(Tl))	wavelength of max. emission [nm]	Rise time [ns]	Decay time [ns]
Anthracene	Crystal	1.25 [28]	50-60 [29]	445 [28]	–	30 [28]
NaI(Tl)	Crystal	3.67 [28]	100	415 [28]	–	230 [28]
CsI(Tl)	Crystal	4.51 [28]	5-6	550 [28]	–	1000 [28]
CsF	Crystal	4.11 [30]	3-5 [30]	390 [31]	0.35 [30]	2800 [30]
BaF$_2$	Crystal	4.88 [32]	16/3 NaI [32]	220/310 [32]	–	0.6-0.8 / 630 [32]
BGO	Crystal	7.13 [33]	25 [33]	480 [33]	–	300 [33]
LSO	Crystal	7.4 [34]	76 [35]	410-420 [35]	–	40 [34]
LYSO	Crystal	7.3 [33]	75 [33]	428 [33]	–	40/44 [33]
Brillance 380	Crystal	5.08 [36]	165 [36]	380 [36]	9 [7]	16 [37]
NE102A	Plastic	1.032 [38]	28 [38]	423 nm [38]	≈0.02 [39]	2.4 ns [38]
BC404	Plastic	1.032 [40]	27-34 [40]	408 [40]	0.7 [40]	1.8 [40]
RP422	Plastic	1.032 [41]	16 [41]	370 [41]	0.35 [41]	1.6 [41]

Table 3.2: Properties of scintillator materials

Scintillator name	Light Output [Photons/MeV]	Att. coefficient for 511 keV photons $[\text{cm}^{-1}]$	Chemical formula	Hygroscopic
Anthracene	20000 [28]	–	$C_{14}H_{10}$ [28]	NO [28]
NaI(Tl)	38000 [5, 42]	0.34 [31]	NaI(Tl)	YES [43]
CsI(Tl)	65000 [5, 42]	0.483 [3]	CsI(Tl)	Slightly [43]
CsF	2000 [44]	0.39 [31]	CsF	NO
BaF_2	1400/9500 [5, 42]	0.44 [3]	BaF_2	Slightly [43]
BGO	8000 [28]	0.96 [3]	$Bi_4(GeO_4)_3$	NO [43]
LSO	25000 [5, 42]	0.87 [3]	LU_2SiO_5	NO
LYSO	32000 [45]	0.87 [3]	$Lu_18Y_2SiO_5(Ce)$	NO [43]
Brillance 380	70000 [46]	0.09 [24]	$LaBr_3(Ce)$	YES [43]
NE102A	10000 [5, 42]	0.0980 [40]	see Tab. 3.3	NO
BC404	10000	0.0980 [40]	see Tab. 3.3	NO
RP422	10000	0.0980 [40]	see Tab. 3.3	NO

3.5 Polymer scintillators

In this section chemical structure of polymer scintillators which were studied in this thesis is discussed. All solid polymer detectors consist of three components: *base* with which incoming photons interact, *primary additive* which absorbs photons from excited base and emits them in energy regime where they cannot be further absorbed by base molecules and secondary additive - *waveshifter*, which again absorbs photons emitted from *primary additive* and "shifts" them into wavelength region where quantum efficiency of photomultiplier is higher. There are many possible choices of mixture of base, primary and secondary additives, each proper for detection of different particles and different energy ranges. In this thesis combinations of two kinds of each component were studied. Their chemical formulas and names can be found in Tab. 3.3. Scintillator samples were connected to the

Table 3.3: Polymer scintillator components studied in this thesis

Component type	Name	Abbreviation
Base	polyvinyltoluene	PVT
Base	polystyrene	PS
Primary additive	2,5-Diphenyloxazole	PPO
Primary additive	p-Terphenyl	PPP
Waveshifter	5-Phenyl-2-[4-(5-phenyl-1,3-oxazol-2-yl) phenyl]-1,3-oxazole	POPOP
Waveshifter	1,4-Bis(2-methylstyryl)benzene	Bis-MSB

Thorn/EMI 9954B photomultipliers. Example signal amplitudes spectrum from one of polymer scintillators is shown in Fig. 3.8. Photomultiplier quantum efficiency as a function of scintillation light wavelength is shown in Fig. 3.9. In the same figure emission spectrum of BC400 scintillator is shown. In this thesis NE102A (an equivalent of BC400) was used to compare spectras of amplitudes from different samples. In Fig. 3.10 quantum efficiency and emission spectrum for scintillator and photomultiplier used in Chapter 6 are shown. Emission wavelength of used scintillators (about 450 nm) matches with quantum efficiency of photomultipliers.
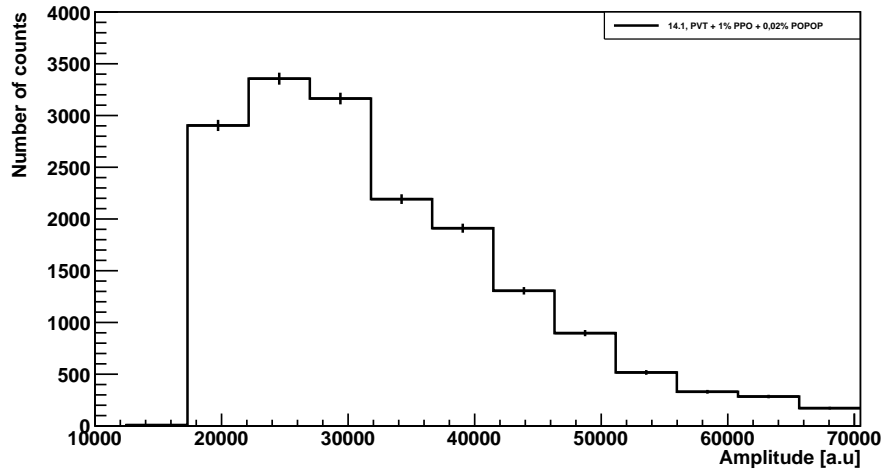
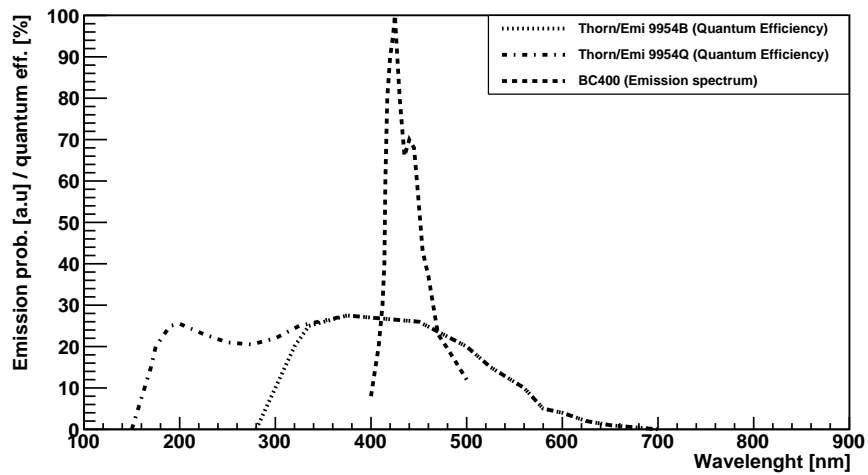Figure 3.8: Example of amplitude spectrum measured for polymer scintillator sample.

Figure 3.9: Quantum efficiency of Thorn/Emi 9954B, 9954QB photomultipliers and spectral response for BC400 scintillator - an equivalent of NE102A.
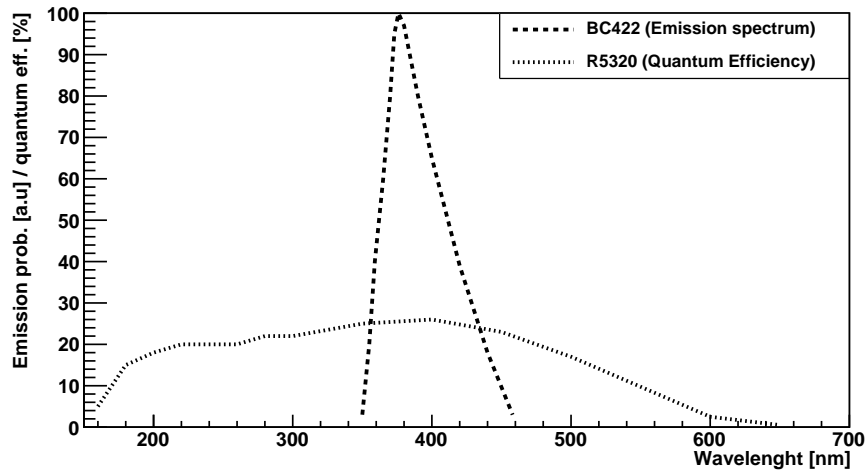
Figure 3.10: Quantum efficiency of Hamamatsu R5320 photomultiplier and spectral response for BC422 scintillator - an equivalent of RP422.

Chapter 4

Estimation of the Compton effect in a patient's body

Gamma quanta from annihilation of positron and electron, traversing through patient's body may be absorbed via photoelectric effect or scattered via Compton effect. If photoelectric effect takes place, γ quantum is lost in patient's body and cannot be detected by PET. However, this is not the case with Compton effect, where γ quanta after scattering can still reach detectors. Those gamma rays can be discarded to some extent by applying energy cut on data before reconstruction. It is important to understand the impact of the value of threshold set on energy of registered signals, on efficiency of aquiring singals when making PET scan, and how this value suppresses the smearing of the reconstruction of the LOR due to the Compton scattering in the patient's body.

4.1 Detector efficiency

When measuring signals from γ rays one must take into account that the efficiency for measuring Compton effect signals will depend on threshold set, as well as the detector thickness. To consider first component one needs to know cross section for Compton scattering expressed in kinetic energy of electron. This can be obtained (see Fig. 4.1 d)) by variables change in equation 3.2.

For the image reconstruction, one takes only this portion of all signals, for which energy of electron is above the threshold value. Ratio of area under line in Fig. 4.1 d) calculated from threshold to 340 keV to the whole area from 0 to 340 keV will be therefore the value of the first component that determines efficiency of detection. Second component needs analysis of absorption of γ rays in matter which is related to the
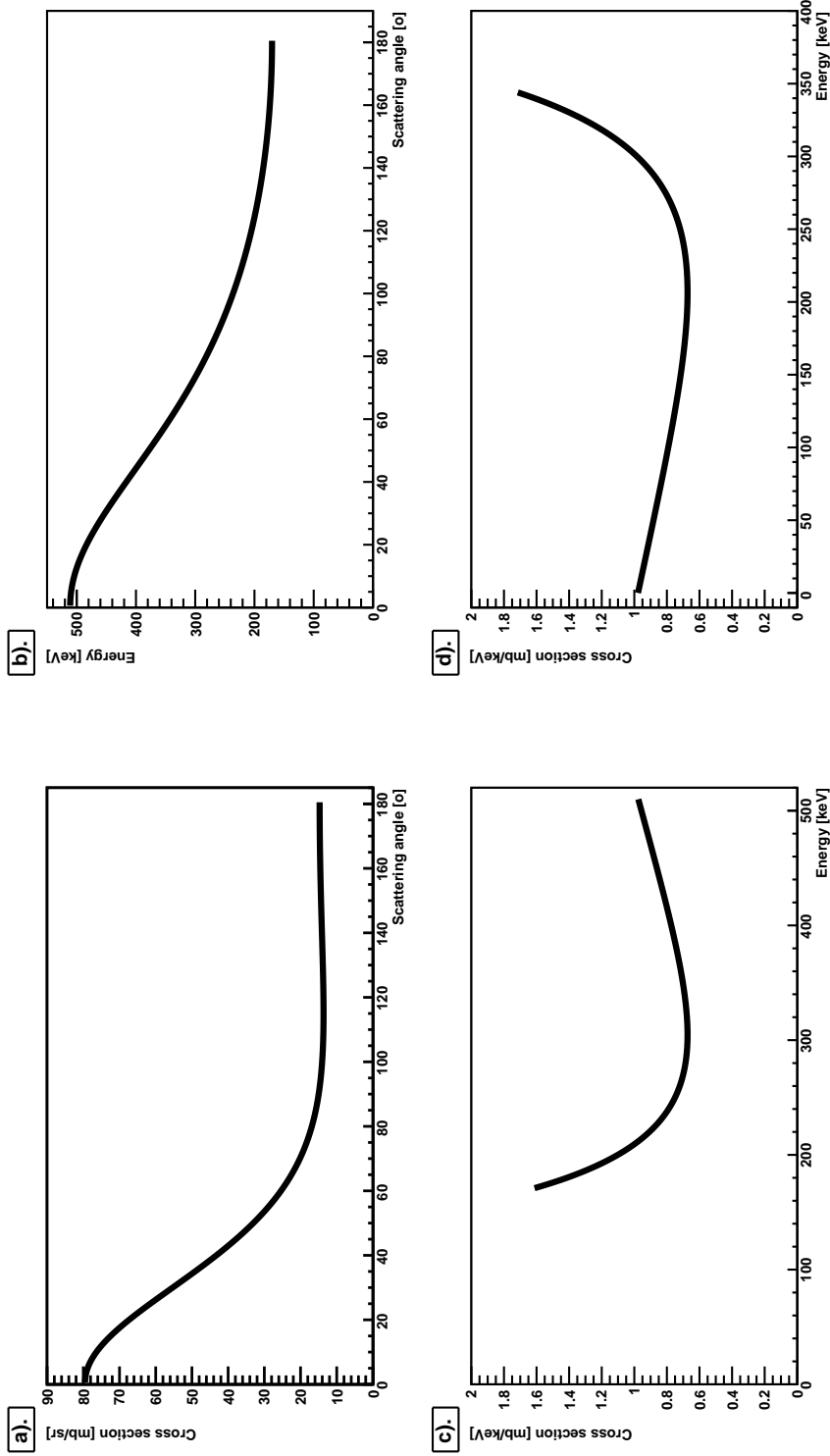
Figure 4.1: a.) Compton effect cross section as a function of scattering angle of photon; b). energy of gamma quantum after scattering on electron as a function of scattering angle; c). Compton effect cross section as a function of energy of scattered photon; d). Compton effect cross section as a function of kinetic energy of scattered electron; with primary energy equal to 511 keV.

thickness of material. This problem is widely discussed in [25].

What one needs to know is a ratio of number of γ rays that did not interact in the detector to the number of those reaching the detector. This proportion can be expressed as:

$$\frac{N}{N_0} = e^{-\mu \cdot x}, \tag{4.1}$$

where x is the thickness of detector, N is the number of γ quanta that passed through without interaction, N_0 stands for the number of γ quanta before passing through and μ denotes a linear absorption coefficient. Example of a typical polymer scintillator is BC404, its linear absorption coefficient is related with cross section for interaction as:

$$\mu = \sigma \cdot D, \tag{4.2}$$

where D is molecular density and σ is cross for Compton effect per molecule. To get the absorption coefficient one needs to first calculate cross section per each molecule. As written in chapter 3, cross section for Compton effect per molecule can be obtained by multiplying cross section per electron by number of electrons in a molecule. Knowing H:C ratio for BC404 which is 1.107 [40], one can get chemical formula for BC404 equal to $C_{10}H_{11}$, which means that each molecule has 71 electrons. Cross section for Compton interaction can be derived by integrating the differential cross section shown in Fig. 4.1 d) from 0 keV to 340 keV. Last number needed is the molecular density for BC404 which can be derived from equation:

$$D = \frac{\rho \cdot n_{AV}}{M}, \tag{4.3}$$

where ρ denotes BC404 density, equal to 1.03 $\frac{g}{cm^3}$ [40], n_{AV} stands for Avogadro number and M denotes molecular mas of BC404 molecule. After such calculation one obtains the attenuation coefficient value equal to: 0.0965 cm^{-1}. What has been derived here is the μ coefficient for reaction in the detector made from BC404.

When one has those two components identified one can plot efficiency of detection as a function of thickness for different energy thresholds. The result is shown in Fig. 4.2.
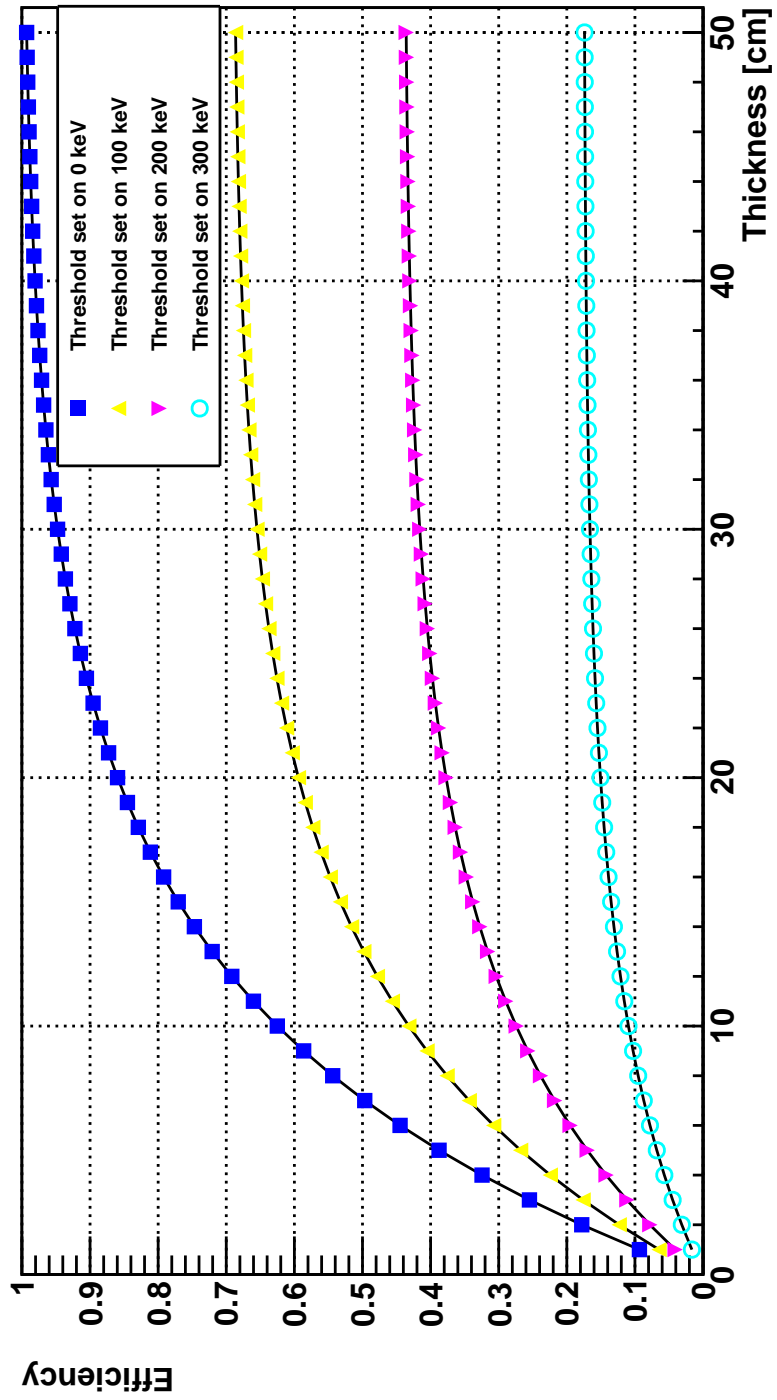
Figure 4.2: Efficiency of detection of Compton signals as a function of detector thickness for different thresholds.

4.2 Energy resolution

Result shown in Fig. 4.1 was obtained under assumption that kinetic energy of electrons is measured by a perfect detector - with no smearing in energy. If one wants to take into account that we use detectors with finite resolution the shape of Compton spectrum will change as shown in Fig. 4.3. What is very interesting in that figure is that, in theory, the spectrum rises rapidly before 340 and ends exactly at 340 keV - the maximum energy electron can acquire from inelastic scattering with γ ray. However, the detector energy resolution is smearing this edge. At 30% smearing the enhancement is no further visible. By comparison of this Monte Carlo simulation and experimental spectrum it is possible to estimate detector energy resolution. In simulation the smearing was
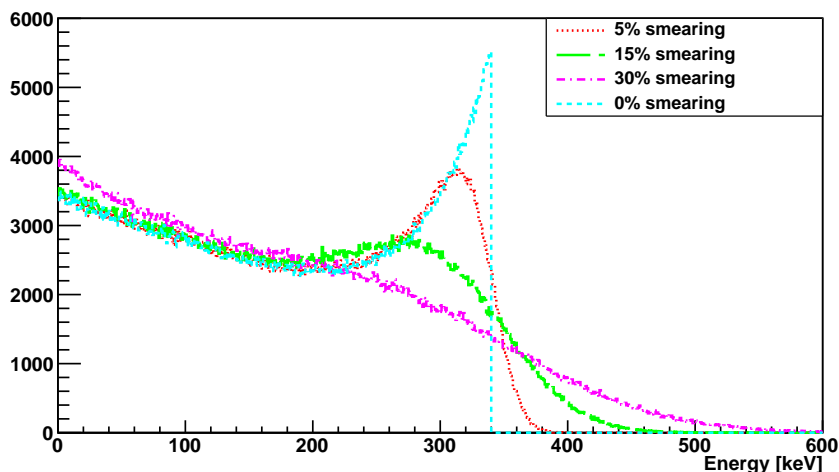
Figure 4.3: Distribution of kinetic energy of electron assuming different energy resolution. Simulation was performed for γ rays of primary energy equal to 511 keV. The smearing indicated in the figure denotes fractional resolution defined as $\frac{\sigma E}{E} \cdot 100\%$

introduced as Gaussian distribution function with standard deviation of $\sigma \cdot E$ which was varying with energy.

4.3 Energy threshold

As shown in Fig. 4.1 there is a direct connection between gamma quanta scattering angle and energy of electrons scattered in Compton effect. Thanks to this one can get rid of fraction of gamma quanta scat-

tered inside a patient's body by adding a cut on energy they deposit in detector. Maximum energy of electron gained through Compton effect is equal to the maximum energy that can be deposited in a detector in one scattering event. This maximum energy is shown in Fig. 4.4 as a function of energy of gamma quanta. The smaller energy of γ quanta the smaller maximum energy which they can deposit in material. From Fig 4.5 in big simplification one can see how setting a threshold on kinetic energy of electrons would decrease the angular range of gamma quanta "background" scattered inside a patient. Gamma quanta unscattered inside a patient can deposit most energy through Compton effect. With higher scattering angle γ quanta have smaller energy, thus deposition of energy via Compton effect in detector will be smaller as well. For instance if one sets threshold on 200 keV for kinetic energy of electron that would allow for acqusition of only those gamma quanta that scattered no more than 60 degrees inside the body as shown in Fig. 4.5. The angular distribution of γ quanta scattered in the pa-
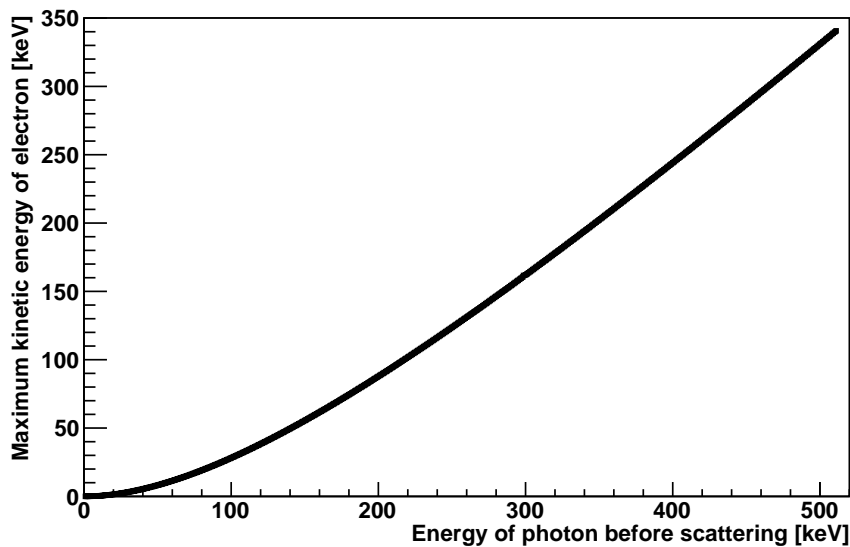
Figure 4.4: Maximum kinetic energy of electron gained through Compton effect as a function of energy of γ quantum before scattering.

tient will not be isotropic. In the following this distribution will be determined for the discussed polymer scintillators and detectors based on Compton effect and it will be compared to the angular distribution of scattered gamma quanta as used in the commercial PET detectors based on photoelectric effect. Points on figure were calculated assuming that probability of detection is proportional to the product of three
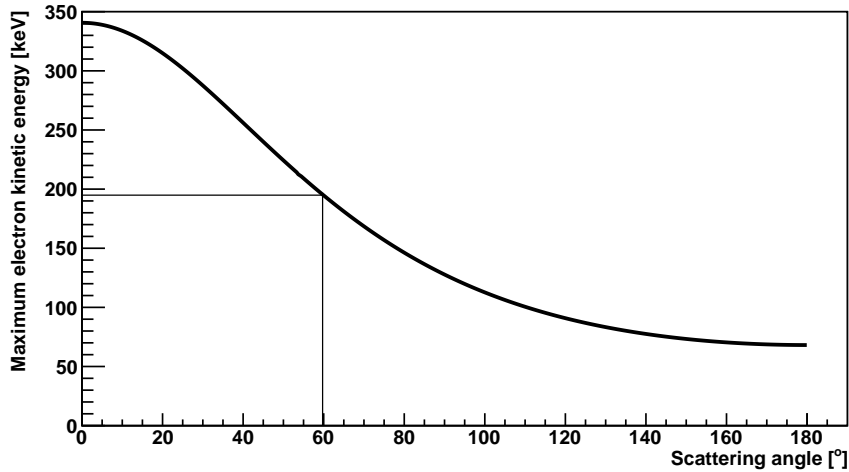
Figure 4.5: Maximum kinetic energy of electron which may be gained through Compton effect in detector as a function of scattering angle of gamma quantum inside patients body.

components. First related to probability for scattering into given angle, which can be derived from Fig. 4.1 a)., second associated with probability of depositing by γ quanta enough energy in detector material to cross energy threshold, which is derived by calculating ratio of Monte Carlo simulated electrons that met this criterion to all simulated electrons (see Fig. 4.6), and third equal to probability of interaction in plastic scintillator of thickness equal to 2 cm, where linear attenuation coefficient was calculated as previously in section 4.1. As one can see gamma quanta scattered into smaller angles will be still detected, while those scattered with angles larger than 60 degrees will be cut by a threshold of 200 keV. This shows that one can effectively choose which γ quanta are to be used in reconstruction by changing threshold. In novel TOF PET detector based on plastic scintillators this method would allow choosing of maximum scattering angle in body of γ quanta used in reconstruction by choosing proper threshold. As a comparison case of detection in LSO crystal has been calculated as well and can be seen in Fig. 4.8. In this case probabilty of detection is proportional to probability of scattering into given angle in patient body multiplied by probability of detection of γ quantum inside 2 cm LSO crystal via photoelectric effect. In the calculations a threshold of 340 keV was applied, corresponding to the enrgy of gamma quanta scattered in the patient by 60°. At present most PET scanners use thresholds set on 300 keV [1], which is an energy that γ quanta can deposit through pho-
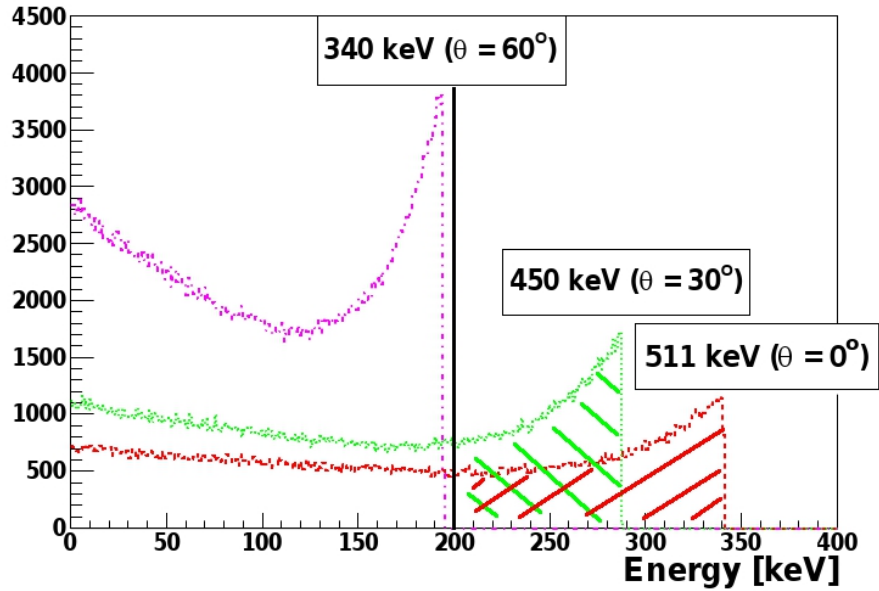
Figure 4.6: Simulated distribution of energy of electrons gained via Compton effect for three different primary energies of γ quanta. Scattering angles corresponding to those energies are written in brackets. Black vertical line illustrates energy threshold, only electrons with energy higher than this threshold are further taken into account. Area under plots divided by number of all simulated events is equal to second component mentioned in text.

toelectric effect even after scattering inside body by about 75°. Above calculations are only an approximation, because of not taking into account energy resolution of detectors. Further studies in this matter will be done after completion of this thesis.

Figure 4.7: Angular distribution of γ quanta scattered in the patient's body as measured by the 2 cm thick plastic scintillator with energy threshold set to 200 keV.

Figure 4.8: Angular distribution of γ quanta scattered in the patients body as measured by the 2 cm thick LSO detector with energy threshold of 340 keV. In the calculation only a photoelectric effect was taken into account.
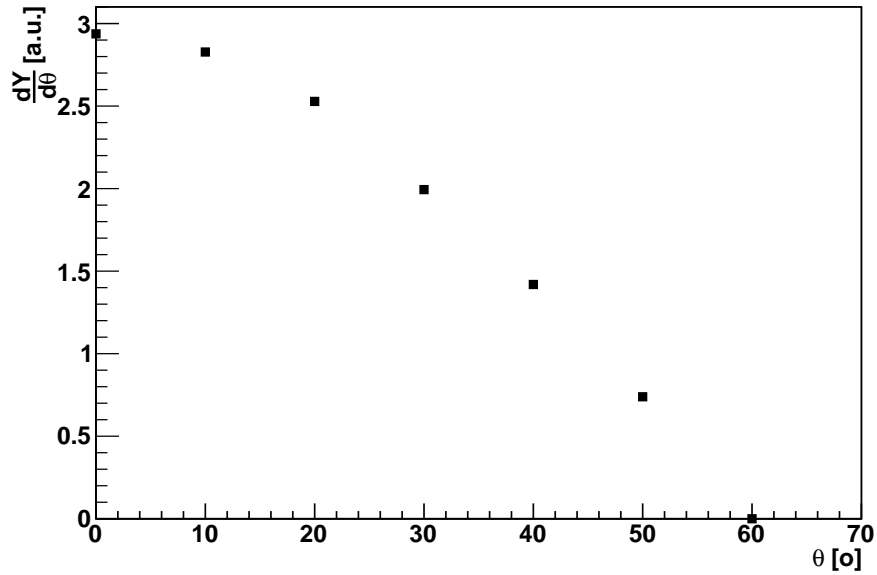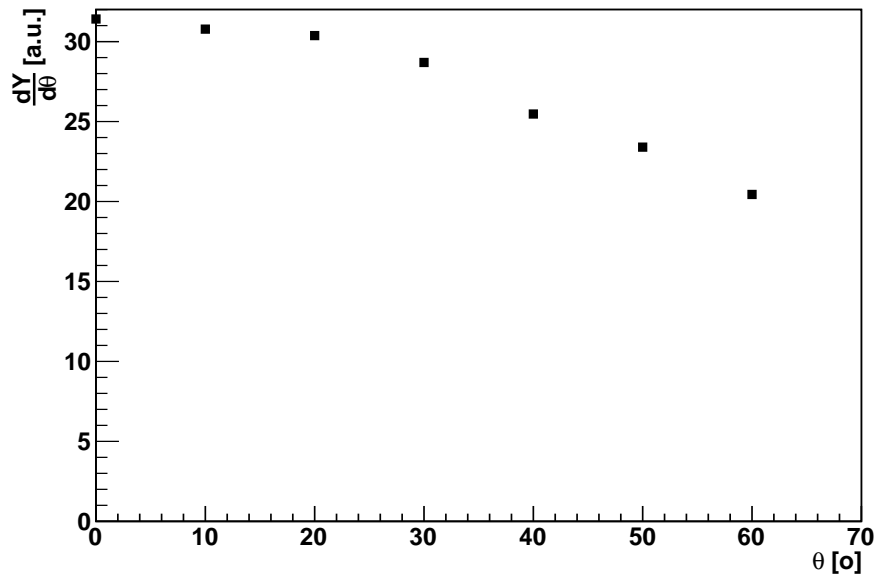
43

Chapter 5

Studies of polymer scintillators

As mentioned in chapter 3 each polymer scintillator consists of three components: base, primary additive and waveshifter. One of the aims of this work was to check which mixture of those three components would give the highest amplitude signals as well as a shape of amplitude spectrum closest to the presently available commercial sample. Samples made by dr A. Kochanowski and Ł. Kapłon [26] were divided into 3 series which are shown in table 5.1.

Table 5.1: List of polymer scintillator samples with the same labels as in [26]. The abbreviations of chemical substances are explained in Tab. 3.3.

Series	Number	Composition of samples
14	1	PVT + 1% PPO + 0.02% POPOP
	2	PVT + 1% PPO + 0.02% bis-MSB
	3	PS + 1% PPO + 0.02% POPOP
	4	PS + 1% PPO + 0.02% bis-MSB
15	1	PVT + 1% PPP + 0.02% POPOP
	2	PVT + 1% PPP + 0.02% bis-MSB
	3	PS + 1% PPP + 0.02% POPOP
	4	PS + 1% PPP + 0.02% bis-MSB
16	1	PVT + 1% PPO + 0.1% POPOP
	2	PVT + 1% PPO + 0.02% bis-MSB
	3	PVT + 1% PPP + 0.02% POPOP
	4	PVT + 1% PPP + 0.02% bis-MSB
	5	PVT+1%PPO+0.1%bis-MSB+0.1%Ce

Each sample had a cylindrical shape with a diameter of 1.5 cm and height of 3 cm. As a reference NE102A sample was used with the same geometrical shape. As a base of the scintillator material two substances were tested: polyvinyltoluene and polistyrene. For primary additives

44

PPO and PPP were used. Selected waveshifters were: POPOP and bis-MSB. Combinations of each base, additive and waveshifter were divided into three series (see table 5.1). Here we use numbers of series as described in [26]. Samples from the 14th series differ from the 15th series only by the first additive. In the 14th series a PPO additive was used and PPP was used in the 15th. In the 16th series the amount of waveshifter was changed from 0.02 % to 0.1%. In addition the sample 16.5 has 0.1% admixture of Cerium.

5.1 Experimental setup

Experimental setup which was used is shown in Fig. 5.1. Sodium source was taped to the bottom of neutral particle detector [11], which was placed above the tested sample. The tested scintillator was connected with optical grease to photomultiplier Thorn/EMI 9954B (see Tab. A.1). Signal from this photomultiplier was transferred to one of the channels of digital oscilloscope (LeCroy Waverunner LT374). To the second channel a cable with signal coming from coincidence unit was connected. Coincidence signals were required from both sides of neutral particle detector. Digital oscilloscope recorded amplitude of
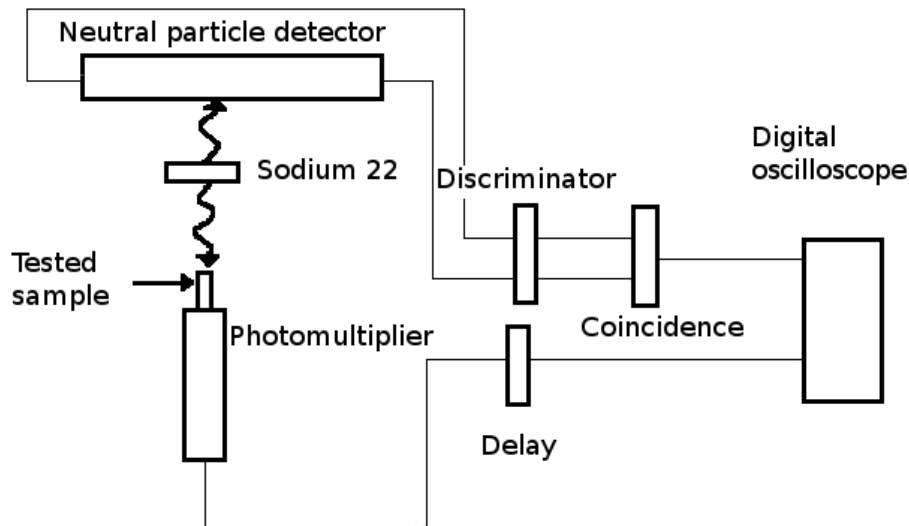

Figure 5.1: Experimental setup used in measuring amplitude spectra of polymer scintillator samples.

the signal from tested sample under condition that it came in a coin-

cidence window of 50 ns. Oscilloscope had an 8-bit Analog to Digital converter which allowed for measuring amplitudes of signals from the tested sample. This experimental setup enables recording only those signals that appeared in all three photomultipliers within 50 ns. For measurements ^{22}Na source was used with activity of about 800 kBq. In practice two sources of 400 kBq joined together were used. This β^+ emitter, allowed making tests with γ quanta originating from e^+e^- annihilation with energy of 511 kV, exactly as used in the PET. In Appendix A more specific informations about experimental setup are gathered.
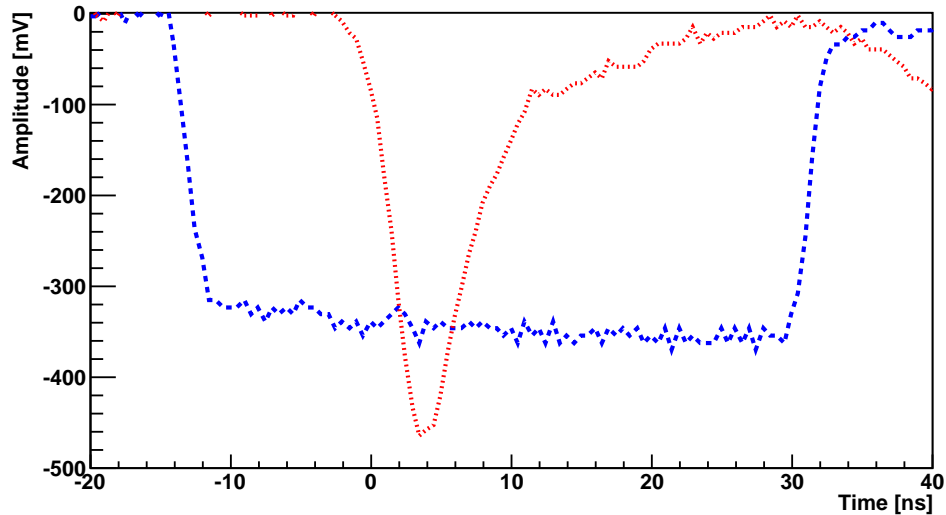
Figure 5.2: Example of a measured signal from the tested sample (red) within coincidence window (blue) of 50 ns width. The picture was taken with LeCroy Waverunner oscilloscope LT374.

5.2   Energy resolution

In theory one could expect an amplitude spectrum that comes from Compton effect (see e.g. Fig. 3.4), but what one can see in practice is a spectrum shown in Fig. 5.3. The difference between theoretical and measured spectrum can be explained by energy resolution of tested detector.

The shape of measured spectrum is a convolution of theoretical shape from Fig. 3.4 and experimental energy resolution. In Fig. 5.4

46

Figure 5.3: Examplary distribution of signal amplitudes as determined for two tested samples.

Figure 5.4: Comparison of result of experimental measurement with distribution of kinetic energy of electrons smeared by 30%. For experiment spectrum the horizontal axis was resized to conform the result of Monte Carlo simulations. Experimental histogram is cut below threshold on amplitude apllied at oscilloscope.

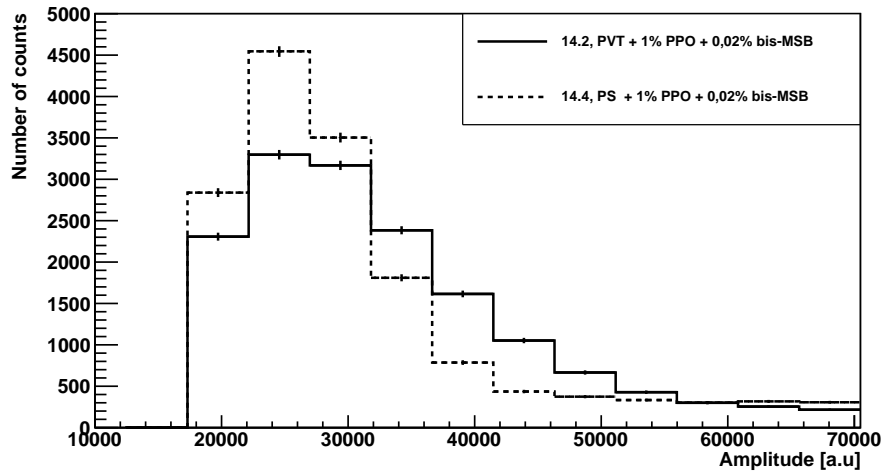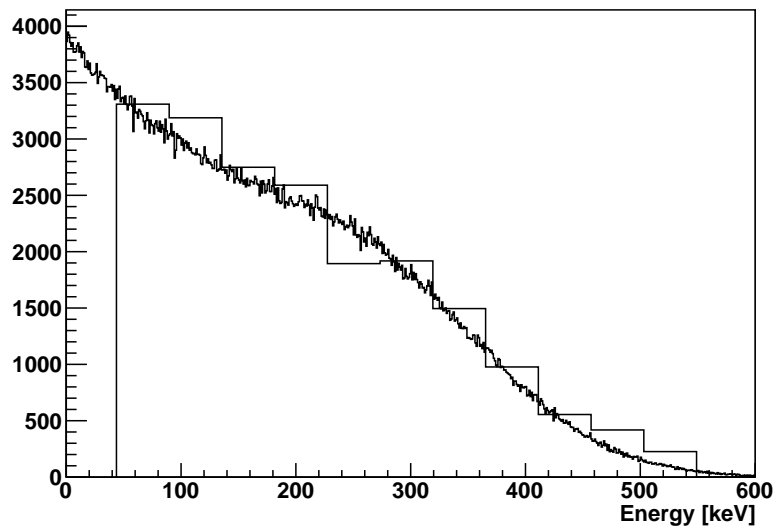energy spectrum simulated assuming 30% energy resolution is compared to experimental result for one of the samples.

The similiar shape of both spectra, indicates that the energy resolution of the tested sample was equal to about 30%.

5.3 Results and comparison with a commercial sample

To extract the best composition of elements showed in Tab. 5.1, amplitude spectra from three hours of measurements per each sample are compared for mixtures differing in only one of components and the two other remaining uchanged. Different combinations of samples are shown in Figs. 5.5, 5.6 and 5.7.

If we consider a sample with signals of higher amplitudes as better, one can find out from histograms that PVT+PPO+POPOP mixture is the best combination of base, primary and secondary additives. Another comparison presented in Fig. 5.8 allows for determining the influence of higher amount of waveshifter in polymer scintillator on an amplitude spectrum.

Every sample from the 16th series has higher amplitude signals than its equivalent from the series 14th or 15th. Which could mean that more photons are shifted into region more efficient for the used photomultiplier. Of course one must take into account that all results were acquired with photomultiplier Thorn/EMI 9954B, and could be different for another one.

Based on the results presented in Fig. 5.8, a sample 16.1 was chosen as the best one. Comparison of energy spectrum of this sample with commercial scintillator NE102A is shown in Fig. 5.9. As the next step after completion of this thesis further tests will be conducted in order to find an even better mixture.

As mentioned in the beggining of this chapter, a sample doped with Cerium was also made [26]. Unfortunately doping did not improve spectrum, it rather decreased the number of high amplitude signals. There could be several reasons for this behaviour. The most probable was the way of inserting Cerium. Doping was done by simply mixing nanopowder with polymer, which resulted in the non-uniform distribution of Cerium inside sample [26]. In the near future the investigations of implementation of Cerium will be continued.
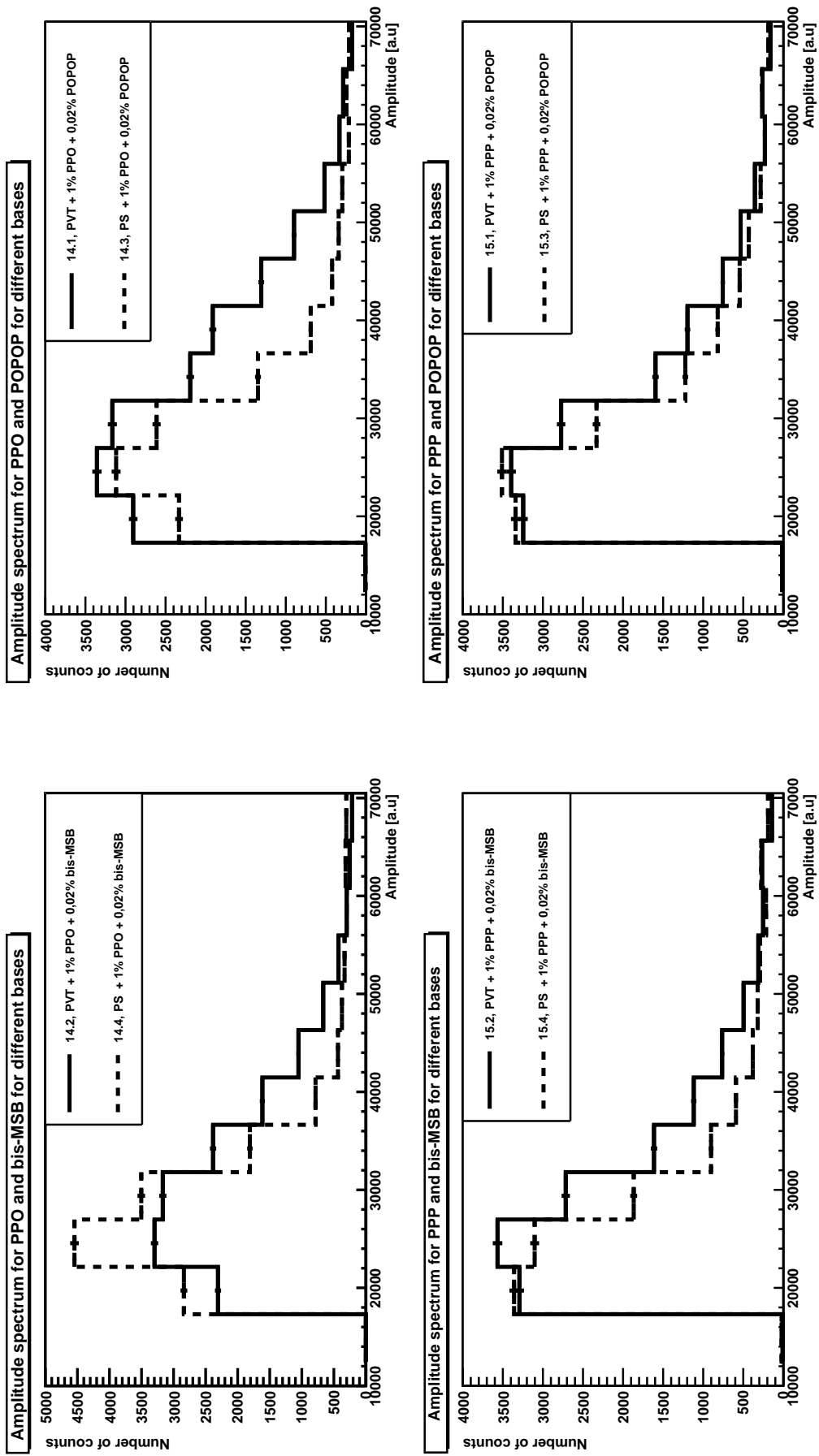
Figure 5.5: Set of histograms for finding the best base.

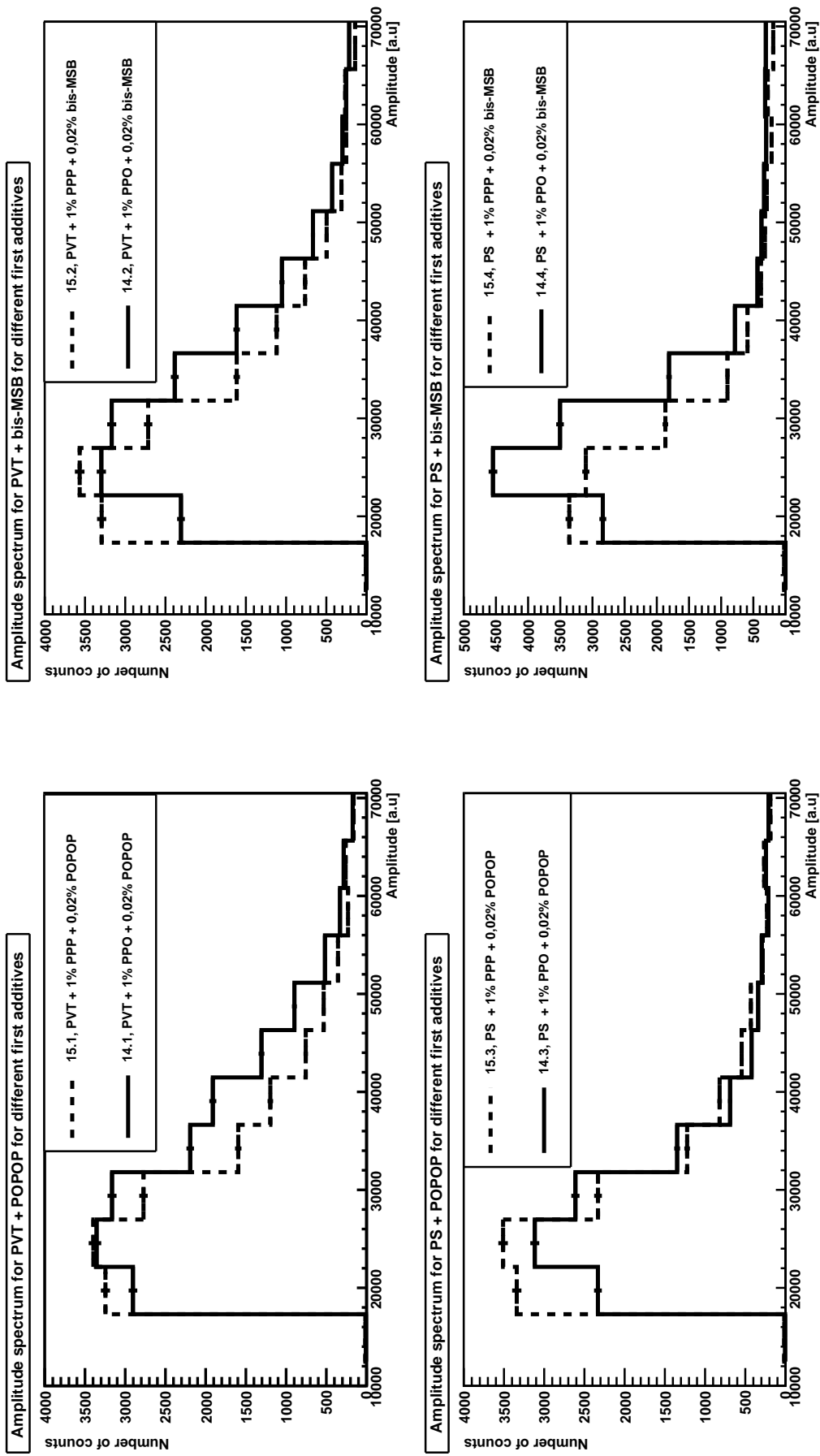Figure 5.6: Set of histograms for finding the best primary additive.
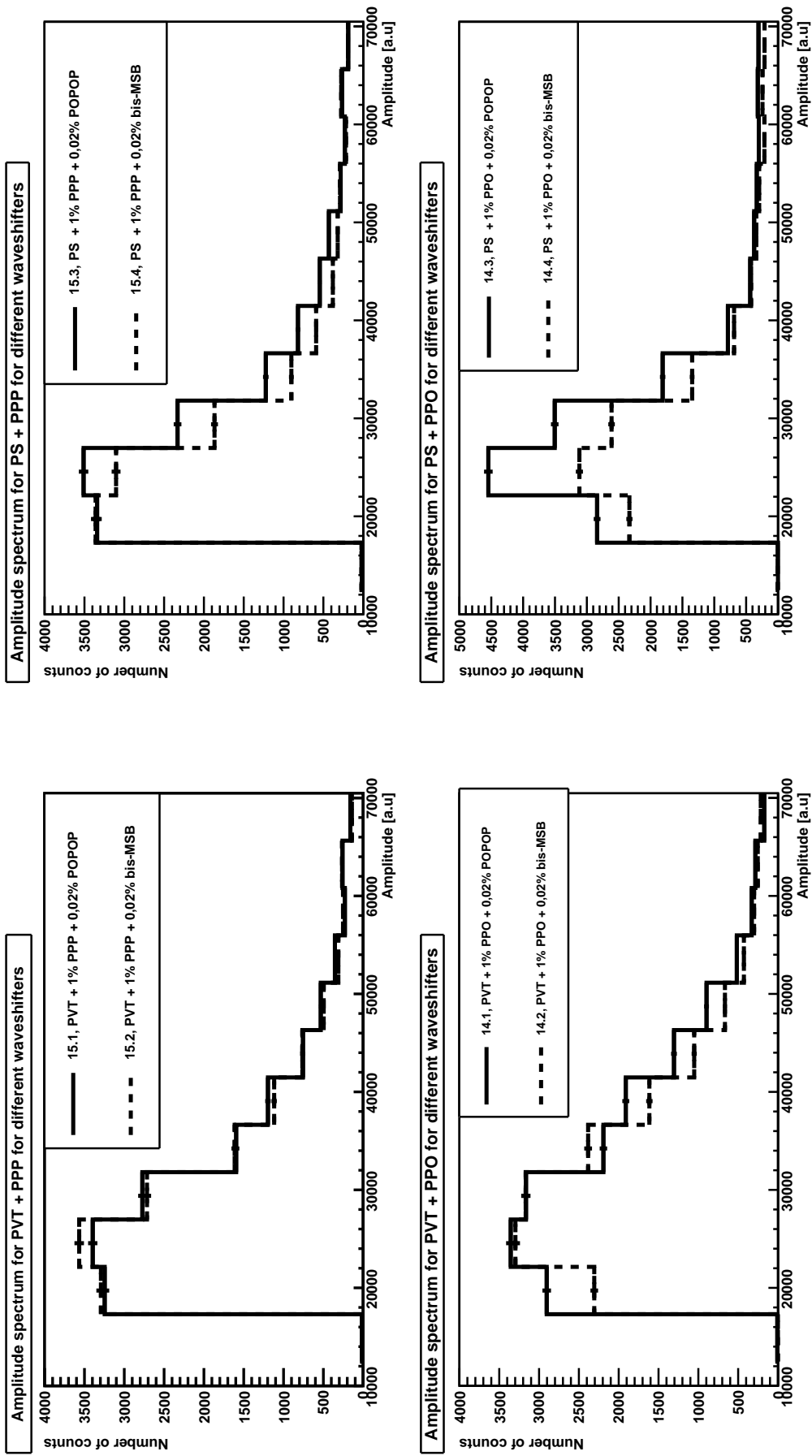
Figure 5.7: Set of histograms for finding the best waveshifter.
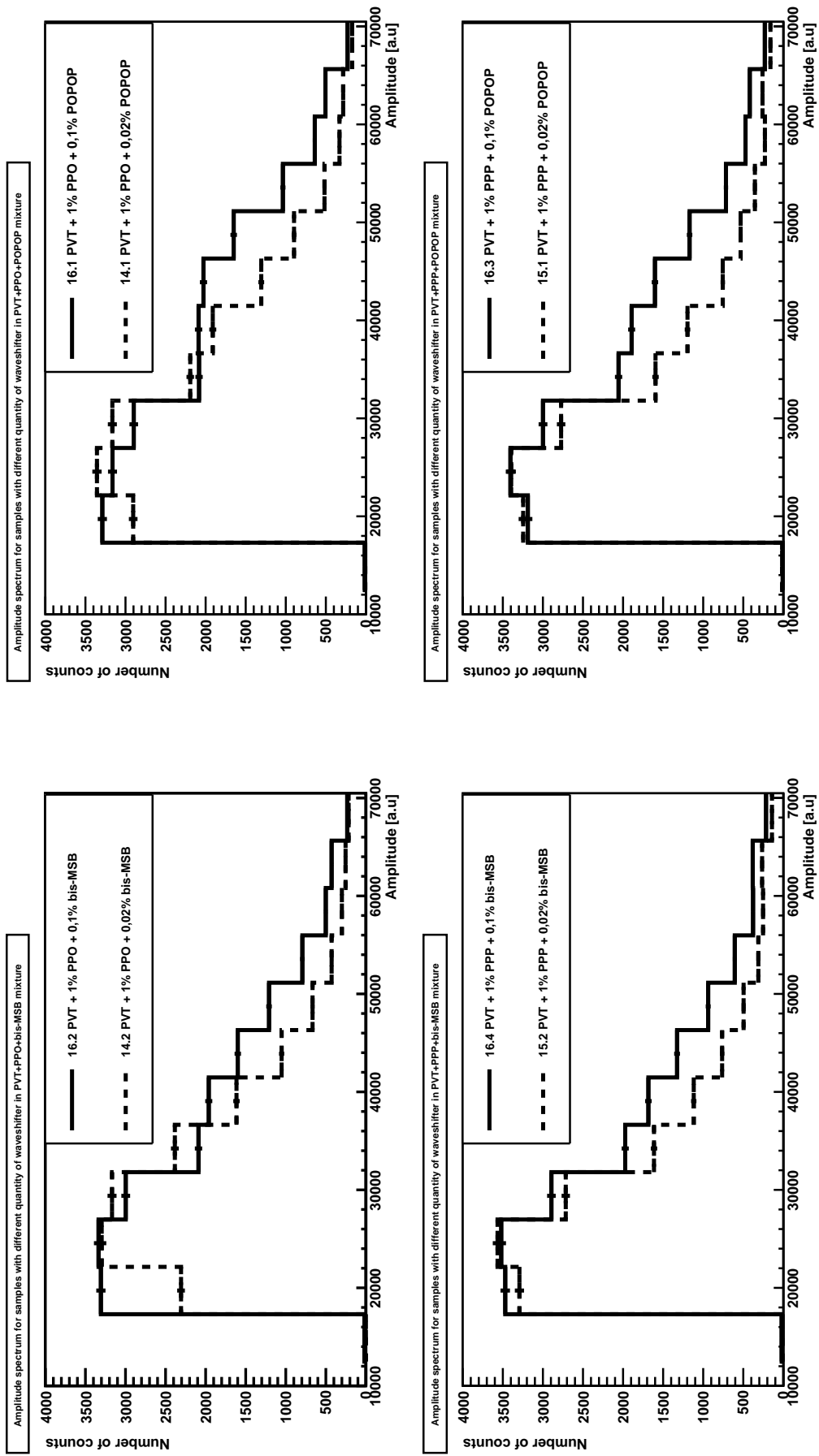
Figure 5.8: Set of histograms for checking influence of increased amount of waveshifter.
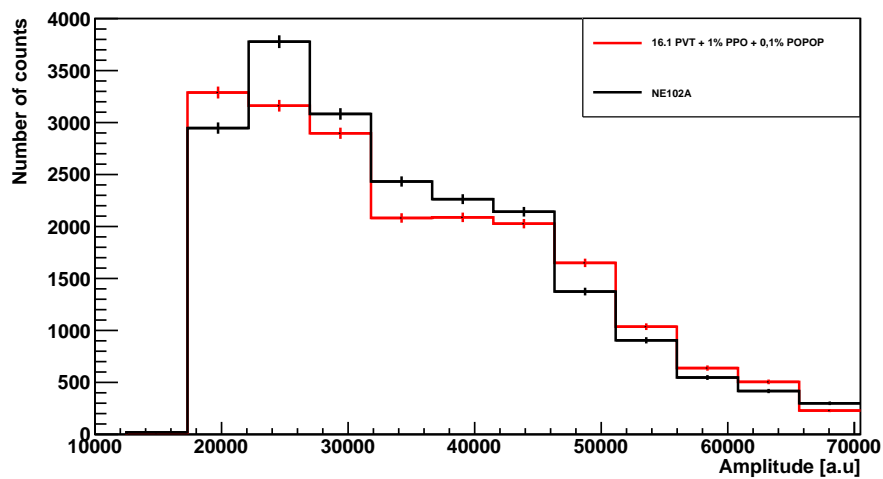
Figure 5.9: Comparison of amplitude distributions measured for 16.1 sample and commercial NE102A.
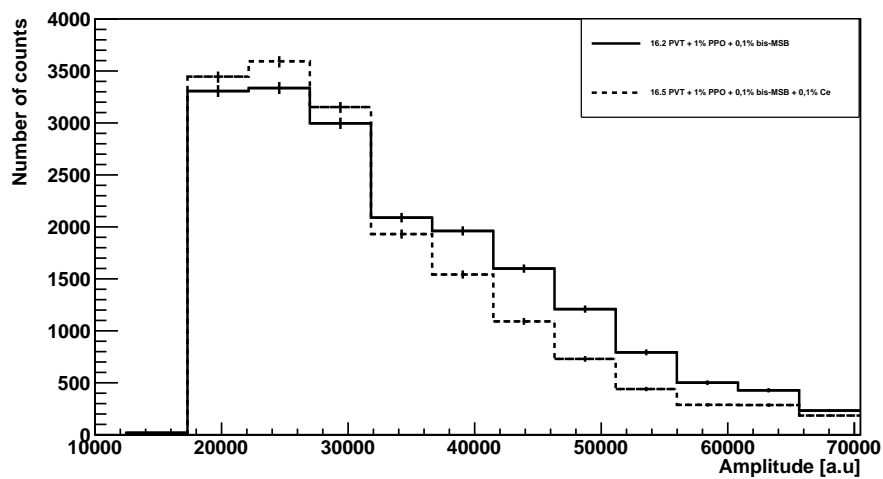
Figure 5.10: Comparison of amplitude spectrum of signals of a sample with and without Cerium

Chapter 6

Studies of time resolution for organic scintillator strip

Fast signals from organic scintillators allow for very precise Time Of Flight measurements. Quantity that describes accuracy of time measurements is called time resolution, the lower it is the better one can establish the difference between two signals.

6.1 Reconstruction of the point of interaction

To measure the time resolution of a detector module which was described in section 2.4 one needs to measure a difference of two time signals originating from reactions of γ quanta at a fixed point of the detector (see Fig 6.1). The measured time (t^{exp}) can be expressed as:

$$t_1^{exp} = t_{real} + \frac{L - x}{v_{eff}} + C_1,$$

(6.1)

$$t_2^{exp} = t_{real} + \frac{x}{v_{eff}} + C_2,$$

(6.2)

where the second term denotes time that a signal needs to travel from a place where a particle hit the detector to a photomultiplier, and a third term indicates time which a signal needs to be analysed and transported through electronics. If we look at the difference between the time of arrival of signals from each side of a module we will get a Gaussian distribution with mean:

$$\Delta t^{exp} = t_2^{exp} - t_1^{exp} = \frac{L - 2x}{v_{eff}}.$$

(6.3)
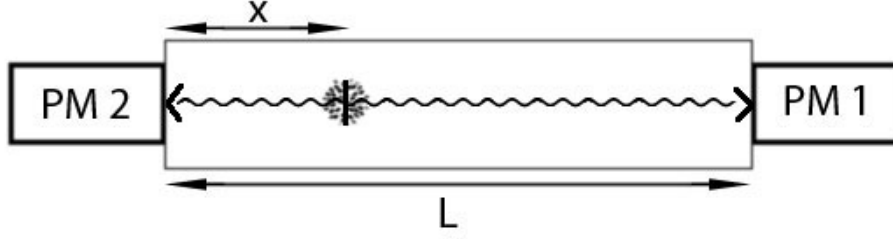
Figure 6.1: Schematic illustration of a single interaction of gamma ray with scintillator detector. Black dot denotes the hit position, x stands for the distance from photomultplier 2.

Average of t_2^{exp} and t_1^{exp} gives us a value which is equal to real time of the hit plus a constant:

$$T = \frac{t_1^{exp} + t_2^{exp}}{2} = t_{real} + C. \tag{6.4}$$

Uncertainty of determining a real time of the hit is then equal to an uncertainty of T. If we use law of statistical uncertainty transfer we get:

$$\delta T = \frac{1}{2}\delta(t_1^{exp} + t_2^{exp}) = \frac{1}{2}\sqrt{(\delta t_1^{exp})^2 + (\delta t_2^{exp})^2}, \tag{6.5}$$

and assuming that uncertainties of both t_1^{exp} and t_2^{exp} are the same:

$$\delta T = \frac{1}{\sqrt{2}}\delta t^{exp}. \tag{6.6}$$

Uncertainty of Δt^{exp} is equal to (again assuming that uncertainties of times of both signals are the same):

$$\delta(\Delta t^{exp}) = \delta(t_2^{exp} - t_1^{exp}) = \sqrt{2}\delta t^{exp}. \tag{6.7}$$

Finally we get that the time resolution of a single module is given by an equation:

$$\delta T = \frac{1}{2}\delta(\Delta t^{exp}). \tag{6.8}$$

Resolution of measuring TOF difference by two detectors is equal to:

$$\sigma(TOF) = \delta(T_2 - T_1) = \sqrt{(\delta(T_2))^2 + (\delta(T_1))^2} = \sqrt{2(\delta T)^2} = \frac{1}{\sqrt{2}}\delta(\Delta t^{exp}) \tag{6.9}$$

where T_2 and T_1 stand for time measured by module 1 and 2 and under assumption that the time resolutions of two detectors are the same.

6.2 Experimental setup

To build the best TOF PET scanner one wants to get the best possible time resolution, thus it is important to use the fastest organic scintillator available. In the case of this thesis RP422 organic scintillator was selected, some of its properties are shown in table B.1. This material provides a very fast signal, but the maximum wavelength of light comming out was near UV region. Because of that Hamamatsu R5320 photomultipliers with bialkali photocathode and synthetic silica window were used. Properties of photomultiplier are gathered in table B.2.
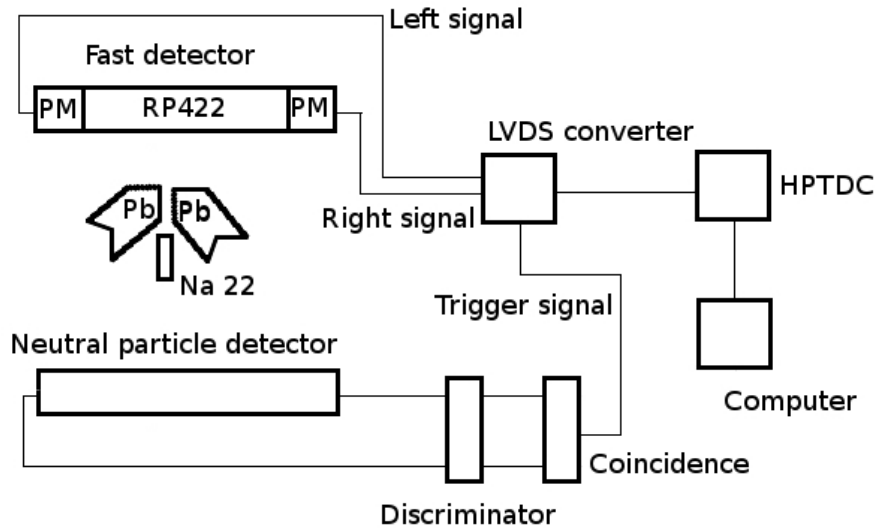
Figure 6.2: Experimental setup used in measuring time resolution of detector constructed from RP422 scintillator and R5320 photomultiplier (fast detector). Neutral particle detector served as a trigger.

To measure time resolution of a strip of RP422 with photomultipliers R5320, connected using optic gel to its both sides, experimental setup shown in Fig. 6.2 was used. Signals from both sides of RP422 were connected directly to analog to LVDS (low-voltage differencial signaling) converter board through 4 ns Lemo cables. This converter was supposed to allow measuring of time and amplitude of signals, making coincidence on the same board and converting them into LVDS standard [47]. Because of prototype construction of the board only the last feature worked properly and signals were converted only when the
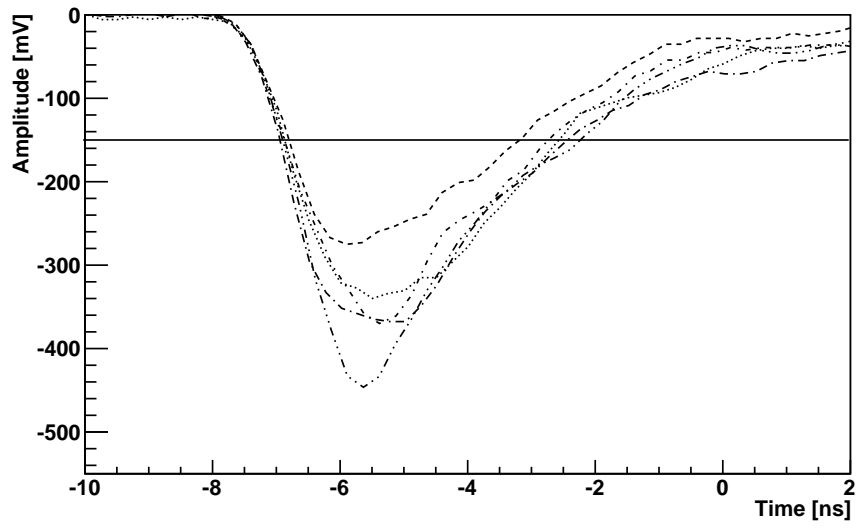
Figure 6.3: Example signals from left part of fast detector. Horizontal black line shows threshold set on signals.
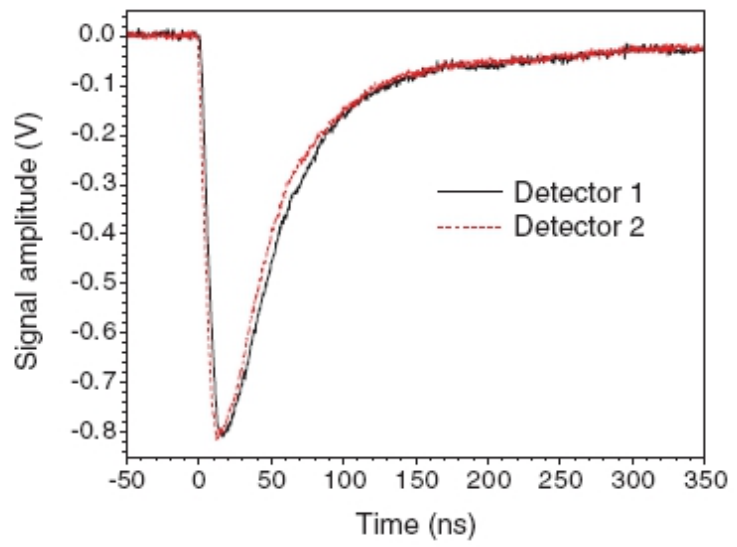
Figure 6.4: Example of signals from Brillance 380 crystal. Figure is adapted from [7].

amplitude was bigger than about 140 mV. More details about the used settings are gathered in Tab. B.3. Convertion was done from first point of crossing threshold to the second one. After conversion, signals were processed by HPTDC (High Performance Time to Digital Converter) and stored in computer data storage. Coincidence signal from both sides of the second detector placed on the other side of radioactive Na 22 source served for the triggering of LVDS converter. This allowed to select only those signals that appeared simultaneously on all 4 photomultipliers. Thus allowing collection of signals comming from annihilation events.
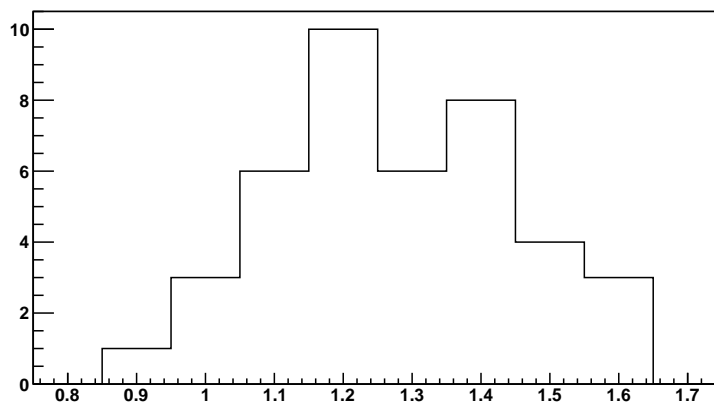
Figure 6.5: Histogram of rise time of signals from Fast detector. Measured rise time of signals is a consequence of rise times of scintillator (0.35 ns), photomultiplier (0.7 ns) and oscilloscope LeCroy Waverunner LT374 resolution of 0.5 ns.

Radioactive source was placed between two lead blocks so that the gamma quanta comming out of it were collimated (as can be seen in Fig. 6.2) at a spot of few milimmeters in the middle of RP422 scintillator. It is possible that γ quanta from the source could interact with the scintillator after comming through lead blocks. Nevertheless considering radiation lenght of gamma rays at energy 511 keV in lead, which is equal to 0.56 cm and the thickness of collimator of 5 cm, those events can be neglected.

In Fig. 6.3 example of signals from RP422 are shown and in Fig. 6.5 their distribution of rising times is presented. Rise tine of about 1.2 ns is almost 8 times smaller than rise time for the fastest crystal detector LaBrillance 380 shown in Fig. 6.4.

6.3 Results

Distribution of time difference of signals from both sides of the fast detector is plotted in Fig. 6.6. To the distribution of time differences Gaussian function was fitted. Standard deviation $\sigma \approx 680$ ps of the fit function corresponds to $\delta(\Delta t^{exp})$ from equation 6.8. Therefore the time resolution of a single module is equal to about 340 ps. Resulting in TOF resolution of about 480 ps. Consequently one gets spatial resolution of about 7 cm. Results are gathered in Tab. 6.1. As one can see the resolution is still very low compared to the result from [7] but there is still a lot of room for improvement. After completion of this thesis the threshold on measured signals will be reduced from about 150 mV to 30 mV. This will be possible after improving LVDS converter board [47]. The decrease of the threshold to 30 mV will improve the time resolution drastically as can be inferred from Fig. 6.7. Time-walk effect will be also taken into account, which should improve time resolution even futher.

Table 6.1: Results

Quantity	Value	Error
Sigma	681,4 ps	10.9 ps
Time resolution of a single module	340,7 ps	5.5 ps
Time resolution of TOF difference	481,8 ps	7,7 ps
Spatial resolution	7,2 cm	0,1 cm
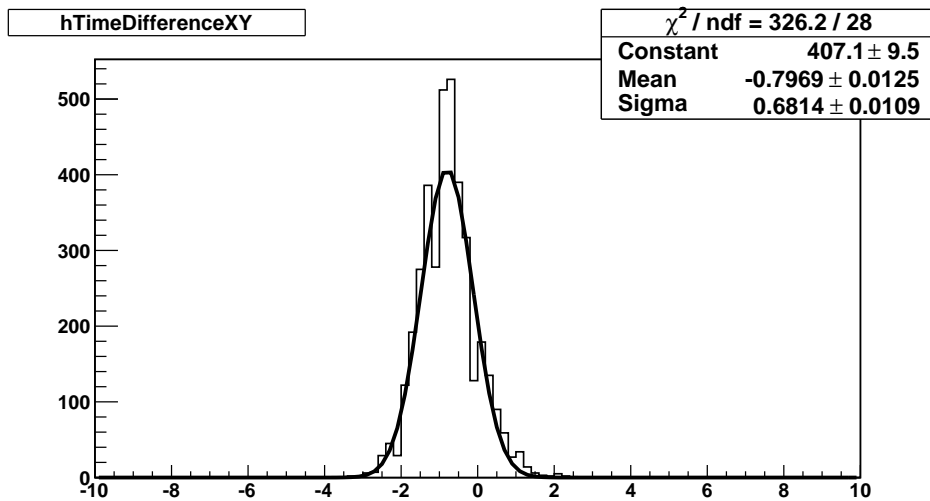
Figure 6.6: Time difference beetween signals from left and right side of scintillator RP422. Units on X axis are ns. Parameters of Gaussian fit are shown in the table in the right-upper side of the figure.
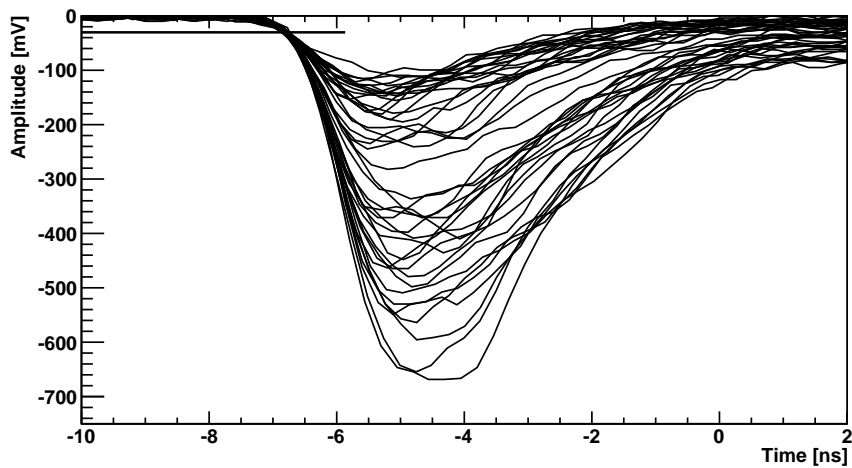
Figure 6.7: Signals measured with LeCroy Waverunner LT 374. Black line shows the desired threshold for measuring signals. In the experiment discussed in this work the threshold was set to about 150 mV.

Chapter 7

Summary and conclusions

The main aim of this thesis was to test the feasibility of using plastic scintillators in construction Time-Of-Flight Positron Emmiting Tomograph.

In the first part of the thesis (chapters 2, 3, 4), TOF PET scanners operation, phenomena connected with this kind of examination, calculations concerning efficiency of detection and simulations of the shape of energy spectrum of electrons gained via Compton effect have been described. In the second, experimental part (chapters 5 and 6), setups used to measure amplitude spectra of different polymer scintillators and time resolution of RP442 organic scintillator have been depicted.

Results from measurements of polymer scintillators allowed for determining the best composition of base, primary and secondary additive to be used in making polymer strips for Strip TOF PET. Each sample had a cylindrical shape with a diameter of 1.5 cm and a height of 3 cm. As a reference NE102A sample was used with the same geometrical shape. As bases of the scintillator material two polymers were tested: polyvinyltoluene and polistyrene. For primary additives PPO and PPP were used. Waveshifters selected were: POPOP and bis-MSB. Combinations of each base, additive and waveshifter were divided into three series.

From comparison of determined amplitude spectra, sample composed of PVT+PPO+POPOP was chosen as the best one. Comparison of this sample with commercial scintillator NE102A revealed that both spectra have the same shape. As the next step after completion of this thesis futher tests will be conducted in order to find an even better mixture.

The shape of these spectra is a convolution of theoretical shape and experimental energy resolution. Comparison of simulation results with experimental measurements, indicates that the energy resolution of the

tested samples was equal to about 30%.

Influence of doping polymer scintillator with Cerium was also made. Unfortunately doping did not improve spectrum, it decreased the number of high amplitude signals. There could be several reasons for this behavior. The most probable was the way of inserting Cerium. Doping was done by simply mixing nanopowder with polymer, which resulted in a non-uniform distribution of Cerium inside sample. In the near future the investigations of implementation of Cerium will be continued.

Time difference obtained for RP442 scintillator strip is equal to: (681.4 ± 10.9) ps. After completion of this thesis, to further improve this result, threshold on measured signals will be reduced from 150 mV to 30 mV. This will be possible after changing LVDS converter board. Time-walk effect will be also taken into account, which should reduce the time resolution even further. It is also possible to change resolution of HPTDC board form 100 ps to 25 ps which should further improve results.

Experimental results presented in this thesis show the properties of organic scintillators manufactured in the Faculty of Chemistry of the Jagiellonian University are comparable with commercial ones and that it is possible to use plastic scintillators strips as detectors in novel TOF PET scanner.

Appendix A

Settings for experimental setup from chapter 5

Table A.1: Properties of 9954B Thorn/Emi photomultiplier [48].

Type	Head-on type
Spectral response	290 to 680 nm
Dynode Structure	Linear-focused
Dynode Stages	12
Gain Typ.	10^6
Rise time [ns]	2
Transit Time Typ. [ns]	41
Transit Time Spread [ns]	3

Table A.2: Settings of experimental setup.

High voltage on "Neutral left"	2100 V
High voltage on "Neutral right"	2050 V
High voltage on "Sample"	1800 V
Thresholds on discriminators	50 mV
Threshold on test signals	150 mV
Trigger window	50 ns
Delay	32 ns
ADC	8 bit

Appendix B

Settings for experimental setup from chapter 6

Table B.1: Properties of RP422 organic scintillator.

Dimensions used in this work [mm]	14x14x100
Rise time [ns]	0.35
Decay time [ns]	1.6
Pulse width [ns]	1.3
Wavelength of max. emission [nm]	370

Table B.2: Properties of R5320 Hamamatsu photomultiplier.

Type	Head-on
Spectral response	160 to 650 nm
Dynode Structure	Linear-focused
Dynode Stages	10
Gain Typ.	$5.7 \cdot 10^6$
Rise time [ns]	0.7
Transit Time Typ. [ns]	10
Transit Time spread [ns]	0.16

Table B.3: Settings of experimental setup.

Voltage on "Fast left"	2100 V
Voltage on "Fast right"	2050 V
Voltage on "Neutron left"	2000 V
Voltage on "Neutron right"	1900 V
Thresholds on discriminators	50 mV
Threshold on fast signals	146 mV (L)/ 188 mV (R)
Trigger window	2000 ns
HPTRB resolution mode	100 ps

Appendix C

Attenuation coefficients

Table C.1: Attenuation coefficients for photoelectric and Compton effects for plastic scintillator. Data taken from [24].

Photon Energy [MeV]	Compton effect [cm²/g]	Photoelctric effect [cm²/g]
1.000E-03	1.582E-02	2.023E+03
1.500E-03	3.129E-02	6.405E+02
2.000E-03	4.787E-02	2.762E+02
3.000E-03	7.796E-02	8.209E+01
4.000E-03	1.009E-01	3.410E+01
5.000E-03	1.173E-01	1.708E+01
6.000E-03	1.289E-01	9.654E+00
8.000E-03	1.441E-01	3.883E+00
1.000E-02	1.541E-01	1.901E+00
1.500E-02	1.690E-01	5.114E-01
2.000E-02	1.767E-01	1.993E-01
3.000E-02	1.814E-01	5.224E-02
4.000E-02	1.804E-01	2.008E-02
5.000E-02	1.774E-01	9.544E-03
6.000E-02	1.738E-01	5.192E-03
8.000E-02	1.663E-01	1.986E-03
1.000E-01	1.591E-01	9.443E-04
1.500E-01	1.439E-01	2.478E-04
2.000E-01	1.321E-01	9.736E-05
3.000E-01	1.151E-01	2.729E-05
4.000E-01	1.032E-01	1.164E-05
5.000E-01	9.425E-02	6.261E-06
6.000E-01	8.718E-02	3.894E-06
8.000E-01	7.659E-02	1.963E-06
1.000E+00	6.888E-02	1.221E-06

Table C.2: Attenuation coefficients for photoelectric and Compton effects for LSO scintillator. Data taken from [24].

Photon Energy [MeV]	Compton effect [cm^2/g]	Photoelctric effect [cm^2/g]
1.000E-03	5.918E-03	3.324E+03
1.500E-03	1.063E-02	1.383E+03
1.588E-03	1.149E-02	1.217E+03
1.588E-03	1.149E-02	1.450E+03
1.614E-03	1.174E-02	2.008E+03
1.639E-03	1.199E-02	2.831E+03
1.639E-03	1.199E-02	3.211E+03
1.736E-03	1.293E-02	3.073E+03
1.839E-03	1.392E-02	2.942E+03
1.839E-03	1.392E-02	3.119E+03
2.000E-03	1.549E-02	2.921E+03
2.024E-03	1.572E-02	2.837E+03
2.024E-03	1.572E-02	3.247E+03
2.140E-03	1.685E-02	2.837E+03
2.263E-03	1.805E-02	2.476E+03
2.263E-03	1.805E-02	2.618E+03
2.375E-03	1.913E-02	2.341E+03
2.491E-03	2.026E-02	2.092E+03
2.491E-03	2.026E-02	2.176E+03
3.000E-03	2.502E-02	1.397E+03
4.000E-03	3.366E-02	6.915E+02
5.000E-03	4.124E-02	3.948E+02
6.000E-03	4.780E-02	2.478E+02
8.000E-03	5.842E-02	1.175E+02
9.244E-03	6.378E-02	8.041E+01

Table C.3: Attenuation coefficients for photoelectric and Compton effects for LSO scintillator. Data taken from [24].

Photon Energy [MeV]	Compton effect [cm^2/g]	Photoelctric effect [cm^2/g]
9.244E-03	6.378E-02	2.068E+02
1.000E-02	6.671E-02	1.686E+02
1.035E-02	6.799E-02	1.538E+02
1.035E-02	6.799E-02	2.102E+02
1.061E-02	6.891E-02	1.980E+02
1.087E-02	6.983E-02	1.865E+02
1.087E-02	6.983E-02	2.152E+02
1.500E-02	8.182E-02	9.399E+01
2.000E-02	9.227E-02	4.377E+01
3.000E-02	1.049E-01	1.462E+01
4.000E-02	1.112E-01	6.632E+00
5.000E-02	1.142E-01	3.572E+00
6.000E-02	1.155E-01	2.148E+00
6.331E-02	1.156E-01	1.848E+00
6.331E-02	1.156E-01	9.626E+00
8.000E-02	1.152E-01	5.206E+00
1.000E-01	1.133E-01	2.874E+00
1.500E-01	1.065E-01	9.570E-01
2.000E-01	9.960E-02	4.362E-01
3.000E-01	8.839E-02	1.465E-01
4.000E-01	7.998E-02	6.950E-02
5.000E-01	7.345E-02	3.996E-02
6.000E-01	6.821E-02	2.593E-02
8.000E-01	6.015E-02	1.362E-02
1.000E+00	5.419E-02	8.552E-03

Table C.4: Attenuation coefficients for photoelectric and Compton effects for BGO scintillator. Data taken from [24].

Photon Energy [MeV]	Compton effect [cm^2/g]	Photoelctric effect [cm^2/g]
1.000E-03	4.741E-03	4.680E+03
1.103E-03	5.573E-03	3.813E+03
1.217E-03	6.540E-03	3.109E+03
1.217E-03	6.540E-03	3.663E+03
1.232E-03	6.674E-03	3.640E+03
1.248E-03	6.811E-03	3.623E+03
1.248E-03	6.811E-03	3.917E+03
1.328E-03	7.526E-03	3.483E+03
1.414E-03	8.301E-03	3.099E+03
1.414E-03	8.301E-03	3.227E+03
1.500E-03	9.082E-03	2.843E+03
2.000E-03	1.370E-02	1.477E+03
2.580E-03	1.901E-02	8.092E+02
2.580E-03	1.901E-02	1.487E+03
2.633E-03	1.949E-02	1.496E+03
2.688E-03	1.998E-02	1.506E+03
2.688E-03	1.998E-02	1.993E+03
3.000E-03	2.271E-02	1.571E+03
3.177E-03	2.420E-02	1.355E+03
3.177E-03	2.420E-02	1.539E+03
3.427E-03	2.629E-02	1.275E+03
3.696E-03	2.842E-02	1.057E+03
3.696E-03	2.842E-02	1.113E+03
3.845E-03	2.953E-02	1.012E+03
3.999E-03	3.075E-02	9.201E+02
3.999E-03	3.075E-02	9.564E+02
4.000E-03	3.076E-02	9.558E+02
5.000E-03	3.781E-02	5.529E+02
6.000E-03	4.402E-02	3.509E+02

Table C.5: Attenuation coefficients for photoelectric and Compton effects for BGO scintillator. Data taken from [24].

Photon Energy [MeV]	Compton effect [cm^2/g]	Photoelctric effect [cm^2/g]
8.000E-03	5.448E-02	1.689E+02
1.000E-02	6.292E-02	9.493E+01
1.110E-02	6.687E-02	7.222E+01
1.110E-02	6.687E-02	1.020E+02
1.221E-02	7.042E-02	7.982E+01
1.342E-02	7.394E-02	6.245E+01
1.342E-02	7.394E-02	1.236E+02
1.500E-02	7.805E-02	9.156E+01
1.571E-02	7.972E-02	8.089E+01
1.571E-02	7.972E-02	1.070E+02
1.605E-02	8.047E-02	1.017E+02
1.639E-02	8.122E-02	9.662E+01
1.639E-02	8.122E-02	1.097E+02
2.000E-02	8.804E-02	6.576E+01
3.000E-02	1.004E-01	2.251E+01
4.000E-02	1.070E-01	1.037E+01
5.000E-02	1.103E-01	5.646E+00
6.000E-02	1.117E-01	3.422E+00
8.000E-02	1.118E-01	1.546E+00
9.053E-02	1.111E-01	1.098E+00
9.053E-02	1.111E-01	4.804E+00
1.000E-01	1.102E-01	3.705E+00
1.500E-01	1.039E-01	1.281E+00
2.000E-01	9.742E-02	5.983E-01
3.000E-01	8.659E-02	2.073E-01
4.000E-01	7.842E-02	1.004E-01
5.000E-01	7.206E-02	5.852E-02
6.000E-01	6.693E-02	3.833E-02
8.000E-01	5.906E-02	2.037E-02
1.000E+00	5.322E-02	1.284E-02

Bibliography

[1] John L. Humm, Anatoly Rosenfeld, Alberto Del Guerra, *"From PET detectors to PET scanners"*, Eur. J. Nucl. Med. Mol. Imaging Vol. 30, No. 11. (2003), 1574-1593.

[2] A.Z. Hrynkiewicz, E. Rokita *"Fizyczne metody diagnostyki medycznej i terapii"*, Wydawnictwo Naukowe PWN, Warszawa 2000, 102 - 111.

[3] G. B. Saha, *"Basics of PET Imaging"*, Springer Science+Business Media, LLC 2010.

[4] J. S. Karp, *"Benefit of Time-of-Flight in PET: Experimental and Clinical Results"*, J. Nucl. Med. Vol. 49, No. 3 (2008), 462-470.

[5] A.T Nassalski, *"Wspólny detektor do tomografii pozytonowej i rentgenowskiej"*, PhD thesis (2010), The Andrzej Soltan Institute For Nuclear Studies.

[6] C. L. Melcher and J. S. Schweitzer, *"Cerium doped lutetium oxyorthosilicate: A fast efficient new scintillator"*, IEEE Trans. Nucl. Sci. Vol 39 (1992), 502-505.

[7] D. R. Schaart, et al., *"LaBr$_3$:Ce and SiPMs for time-of-flight PET: achieving 100 ps coincidence resolving time"*, Phys. Med. Biol. Vol. 55 (2010), N179-N189.

[8] M. Conti, et al., *"First experimental results of time-of-flight reconstruction on an LSO PET scanner"*, Phys. Med Biol. Vol. 50, 4507-4526 (2005).

[9] P. Moskal, et al., Phys. Rev. C79 (2009), 015208.

[10] G. Amelino-Camelia, et al., Eur. Phys. J. C68 (2010), 619.

[11] S. Branksiepe, et al., Nucl. Instr. Meth. A376 (1996), 397.

[12] M. Dahmen, et al. Nucl. Instr. Meth. A348 (1994), 97.

[13] P. Moskal, Patent Application No: P 388 555 [WIPO ST 10/C PL 388555] (2009), PCT/PL2010/00062 (2010).

[14] P. Moskal, S. Niedźwiecki, M. Silarski, J. Smyrski, J. Zdebik, M. Zieliński, *"Novel detector systems for the Positron Emission Tomography"*, Bio-Algorithms and Med-Systems, suplement No. 1, Vol. 6, No. 12 (2010), 142.

[15] P. Moskal, *"Nuclear physics in medicine, minefield and kitchen"*, Annales Universitatis Mariae Curie-Sklodowska Lublin - Polonia Vol. LVIII (2011), in print.

[16] Jerzy Dryzek *"Wstęp do spektroskopii anihilacji pozytonów w ciele stałym"*, Wydawnictwo UJ, Cracow (1997), 11-28.

[17] Donald H. Perkins *Wstęp do fizyki wysokich energii*, Wydawnictwo Naukowe PWN, Warszawa 2004, 105 -108.

[18] E. Czaicka, *Liniowy model pozytonowego tomografu emisyjnego*, Diploma thesis (2008), Jagiellonian University, Department of physics.

[19] M. Conti, *"State of the art and challenges of time-of-flight PET"*, Physica Medica Vol. 25 (2009), 1-11.

[20] S. Surti, et. al, *"Performance of Philips Gemini TF PET/CT scanner with special consideration for its time-of-flight imaging capabilities."*, J. Nucl. Med. Vol 48(3) (2007), 471-480.

[21] M. Egger, Philips presentation, *"GEMINI TF. For the benefit of patients and caregivers: Advanced physics in a simple box"*.

[22] A. Biegun, Uniwersytet Techniczny w Delft, RD&M, Netherlands, *"Obrazowanie w terapii protonowej za pomocą pozytronowej tomografii emisyjnej"*, lecture in Jagiellonian University.

[23] W. R. Leo, *"Techniques for Nuclear and Particle Physics Experiments"*, Second Revised Edition, Springer-Verlag.

[24] M.J. Berger, et al. *"NIST Standard Reference Database 8 (XGAM)"*, http://www.nist.gov/pml/data/xcom/index.cfm.

[25] A. Strzałkowski, *"Wstęp do fizyki jądra atomowego"*, PWN.

[26] L. Kaplon, *"Polymeryzacja w masie styrenu i jego pochodnych jako materiału do konstrukcji scyntylatorów"*, Diploma thesis (2010), Jagiellonian University, Faculty of Chemistry.

[27] H. Peng, *"Radiation & Radioisotope Methodology"* Lecture 4, Med. Phys., 4R06/6R03.

[28] Scintillating Products Data Sheet, Detec-rad Scintillateurs (2006).

[29] Scintillation Products Data Sheet, Saint-Gobain Ceramics & Plastics (2011).

[30] M. Moszynski, et. al, *(*"Properties of CsF, a Fast Inorganic Scintillator in Energy and Time Spectroscopy"), Nuclear Instruments and Methods Vol. 179 (1981), 271-276.

[31] R. Allemand, *"Potential Advantages of a Cesium Fluoride Scintillator for a Time-of-Flight Positron Camera"*, J. Nucl. Med. Vol. 21 (1980), 153-155.

[32] BaF_2 Barium Fluoride Scintillation Material Data Sheet, Saint-Gobain Ceramics & Plastics (2008).

[33] BGO, GSO, LYSO Data Sheets, Omega Piezo webpage `http://www.omegapiezo.com/crystal_scintillators.html`.

[34] R. Valentini, et. al, *"PAC studies with LSO scintillation crystals"*, Nuclear Instruments and Methods in Physics Research Vol. A623 (2010), 1002-1008.

[35] V.V. Avdeichikov, et. al, *"Light output and energy resolution of CsI, YAG, GSO, BGO and LSO scintillators for light ions"*, Nuclear Instruments and Methods in Physics Research Vol. A 349 (1994), 216-224.

[36] Brillance 380 Data Sheet, Saint-Gobain Ceramics & Plastics (2007)

[37] G. Bizarri, P. Dorenbos, *"Charge carrier and exciton dynamics in LaBr3:Ce3+ scintillators: experiment and model"*, Phys. Rev. B Vol. 75 (2007), 184302.

[38] S. Usuda, et al. *"Phoswich detectors combining doubly or triply ZnS(Ag), NE102A, BGO and/or NAI(Tl) scintillators for simultaneous counting of α, β and γ rays"*, Nuclear Instruments and Methods in Physics Research Vol. A 340 (1994), 540-545.

[39] A.J. Campillo, *"Fluorescence risetime of NE 102 scintillator"*, Nuclear Instruments and Methods Vol 120 (1974), 533-534.

[40] Scintillation Products Data sheet, Saint-Gobain Ceramics & Plastics (2011).

[41] Rexon Data Sheet, private communication.

[42] Glenn. F. Knoll, *"Radiation detection and measurements"*, 3rd ed., John Willey & Sons, Inc., New York, 2000.

[43] Scintillator Products, Saint-Gobain Ceramics & Plastics (2009).

[44] S.E. Derenzo, et. al, *"The quest for the ideal inorganic scintillator"*, Nuclear Instruments and Methods in Physics Research A Vol. 505 (2003), 111-117.

[45] LYSO Data Sheet, Hilger Crystals, `http://www.hilger-crystals.co.uk/properties.asp?material=18`.

[46] J. T. M. de Haas, P. Dorenbos, *Advances in yield calibration of scintillators*, IEEE Trans. Nucl. Sci. Vol. 55 (2008), 1086-92.

[47] K. Łojek, private communication.

[48] 52 mm (22 ") photomultiplier 9954 B series data sheet, Electron Tubes (2007).